

AD-A143 467

MANIPULATION OF THE MIXING PROCESS BETWEEN STREAMS OF
DIFFERENT VELOCITY A. (U) TEL-AVIV UNIV (ISRAEL) SCHOOL
OF ENGINEERING S EINAV SEP 83 DAJA37-88-C-0645

1/1

UNCLASSIFIED

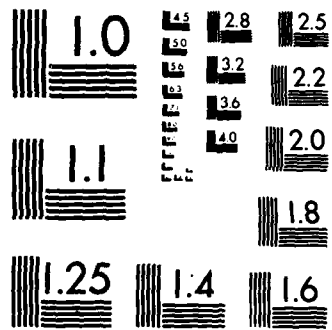
F/G 12/1

NL

END

FBI

ETC



MICROCOPY RESOLUTION TEST CHART
NATIONAL BUREAU OF STANDARDS-1963-A

AD-A143 467



אוניברסיטת תל-אביב
הפקולטה להנדסה

Contract No.

DACA 87-80-0-0001

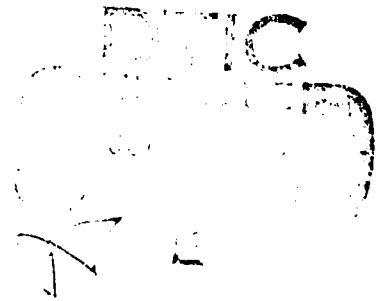
Annual

Report

Oct. 1962 - Sep. 1963

TEL-AVIV UNIVERSITY
SCHOOL OF ENGINEERING
Tel-Aviv, Israel

This document has been approved
for public release and sale; its
distribution is unlimited.



Manipulation of the Mixing Process Between Streams
of Different Velocity and Temperature in
the Presence of Pressure Gradient

Dr. Shmuel Einav
Tel Aviv University

Contract No.

DA JA 37-80-C-0645

Annual

Report

Oct. 1982 - Sep. 1983

DTIC
SELECTE
JUL 27 1984
S D E

The research report in this document has been made possible through the support and sponsorship of the U.S. Army-European Research Office. This report is intended only for the internal management use of the Contractor and the U.S. Government.

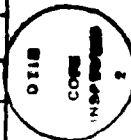
This document has been approved
for public release and its
distribution is unlimited.

Contents

	page
Chapter 1 - Introduction	1
Chapter 2 - Data Acquisition and Numerical Calculations	4
2.1 Phase-locked averaged velocity components	4
2.2 Reynolds stress	6
2.3 Vorticity field	8
2.4 Streaklines	8
Chapter 3 - The Disturbed Mixing-Layer	12
3.1 Streaklines	12
3.2 Vorticity field	14
3.3 Reynolds stress and power spectra	16
References	24

Figures

Accession For	
NTIS GRA&I	<input checked="" type="checkbox"/>
DTIC TAB	<input type="checkbox"/>
Unannounced	<input type="checkbox"/>
Justification	<i>pl</i>
<i>form 50</i>	
By _____	
Distribution/	
Availability Codes	
Dist	Avail and/or Special
<i>A-1</i>	



Chapter 1

Introduction

The aim of this phase of the project was to create a tool for linking the flow-pictures of the disturbed two-dimensional mixing-layer and the phase-locked averaged data calculated from experimentally measured velocity signals. We could thus relate the quantitative analysis of our experimental data to the visually observed phenomena. Of particular interest is the presence of a pairing process of vortices in the experimental data.

There are two theoretical approaches to deal with the mixing-layer type of flow. One is based upon stability theory, and the other tries to solve the basic flow equations by various mathematical models.

Corcos and Sherman (1976) created a numerical model, and used it to examine the roll up process of the shear layer into a vortex. They produced a series of graphs showing iso-dynes (iso-vorticity contours) and streamlines, forming a "Cat Eye" structure, with a vorticity concentration inside, connected to its neighbours by vorticity concentrated braids. Acton (1976) suggested a model, consisting of vortex elements which produced the definition required to observe the evolution and coalescence of the large eddies. Ashurst (1976) employed the method of discrete vortices in order to simulate the two-dimensional mixing-layer. He produced a series of streakline patterns, showing the time development of the mixing-layer.

Riley and Metcalfe (1980) performed direct numerical simulations of the non-linear Navier-Stokes equations with pseudospectral numerical methods. They employed no explicit turbulence modelling, and succeeded in modelling the vortex-pairing mechanism. They found that the presence of the out-of-phase subharmonic of the most unstable linear eigenmode, is essential for the vortex pairing roll-up process. By eliminating the subharmonic, mixing-layer growth stops and negative turbulent energy production occurs, along with a countergradient momentum flux. They suggested that in the laboratory experiments, the out-of-phase subharmonic is suppressed significantly, delaying vortex pairing.

Inoue (1983) simulated turbulent mixing layers by a discrete vortex method obtaining streaklines of fluid particles as well as those of vortices. He found two stages in the development of the mixing layer: a stage of clustering where the vortices interact with each other and tend to form separate clusters of discrete vortices, and a vortex pairing stage. He compared his results with experiments and found them to be in good agreement both qualitatively and quantitatively.

The other physical quantity to be utilized is the stability. Michalke (1964, 1965) used this approach to predict the temporal and spatial growth of disturbances in an inviscid two-dimensional mixing-layer, approximating the mean-velocity nature by a hyperbolic-tangent profile. His results show the roll-up of a vortex, both by iso-vorticity contours and streaklines. Monkevitz and Huerre (1982) studied the influence of the velocity ratio on the spatial instability of mixing-layers, using both hyperbolic-tangent and

Elausius mean-velocity profiles. They found that the maximum growth-rate is approximately proportional to the velocity ratio. Crighton and Gaster (1976) used the multiple-scales expansion method to analyze the development of a slowly-diverging jet flow. Gaster, Kit and Wagnanski (1984) applied the same method to the two-dimensional mixing-layer, approximating the mean-velocity behaviour by modified hyperbolic-tangent profiles, and showed an agreement between the mixing layer growth-rate results thus obtained, and experimental results in the weakly-disturbed turbulent mixing-layer. They also showed the similarity between the eigenfunction profiles, of both the amplitude and phase, to the stream-wise velocity component.

In this report we will compare both the longitudinal and lateral velocity components, as well as the vorticity distribution, using the multiple-scales expansion method. Simultaneous measurements of two velocity components formed the experimental basis for this comparison.

Chapter 2

Data Acquisition and Numerical Calculations

The first step in the numerical computations was to translate the voltages, recorded on the magnetic tape during data acquisition, to the two velocity components, using the calibration coefficients. This procedure produced the instantaneous values of Q and α , and the velocity components U and V were calculated from the following relations:

$$U=Q \cos(\alpha) \quad \text{and} \quad V=Q \sin(\alpha).$$

2.1 Phase-locked averaged velocity components

The phase-locked averaged velocity vectors were calculated from the sampled velocity vectors, in order to analyze the periodic flow phenomena, having the disturbance frequency, or its first subharmonic.

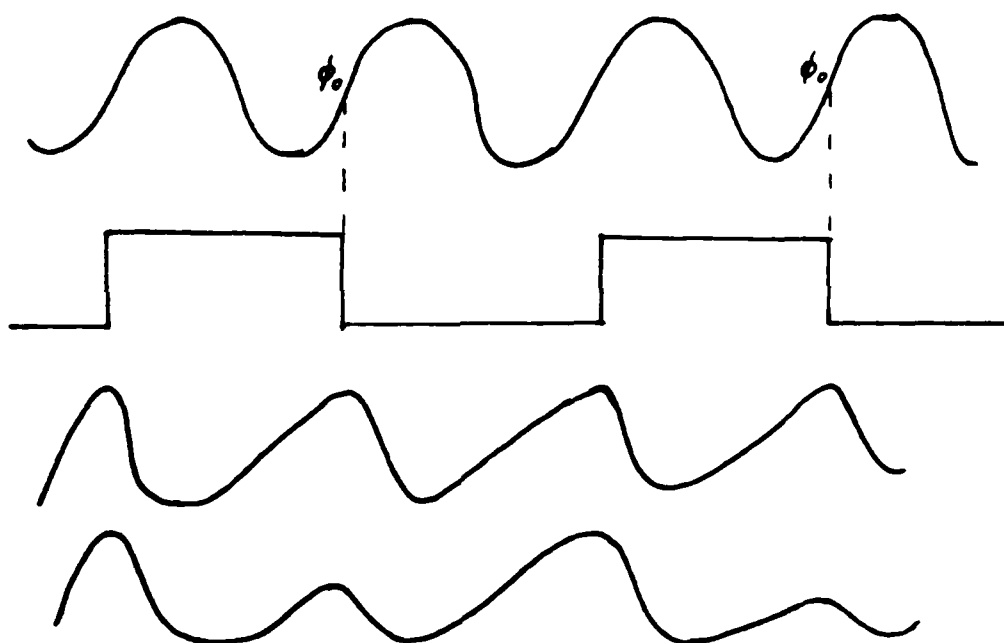
The numerical representation of the phase-locked averaged signal is:

$$\langle U(j) \rangle = \sum_{i=1}^N u(\phi_0 + (j-1)\Delta t + i \cdot \text{NPP})$$

Where u is the original vector containing the velocity values sampled, Δt is the time interval between data points, NPP is the number of data points in each time-period (T) of the frequency analyzed (i.e. $\text{NPP} = T / \Delta t$), ϕ_0 is an arbitrary initial phase, and N is the number of time-periods of the analyzed frequency, contained within the original velocity vector.

The determination of ϕ_0 and NPP required the simultaneous sampling and recording of both the sine-wave signal activating the oscillating flap, and its first subharmonic signal, produced by the electronic frequency-divider circuit, designed to produce a synchronized square-wave signal.

The following sketch illustrates the phased-locked averaging method.



The initial phase points ϕ_0 were defined as the cross points of the subharmonic square-wave signal, having a negative slope, with the zero-voltage level, and NPP was calculated as the mean number of data points between two adjacent initial-phase points.

The result of an averaging process of a signal, dominated by a certain frequency (a fundamental frequency), phase-locked averaging it with respect to its first subharmonic, is a signal having the subharmonic's time-period,

containing two consecutive signals of the fundamental's time-period. All high frequency interferences (turbulent behaviour) are filtered out. If the subharmonic's behaviour is phase-locked to the fundamental frequency, the two signals would be different from one another (shown schematically as [d], in the sketch above). A non-phase-locked subharmonic behaviour, or its non-existence, would produce identical fundamental signals [e].

The length of each sampled velocity vector was 512 points (equivalent to a period of 0.25 sec), and 100 such vectors were acquired. Thus, the subharmonic phase-locked average was calculated from 400 events.

Other flow parameters, such as the mean velocity profiles, the R.M.S. values and the Reynolds stresses, were calculated from the original time dependent velocity vectors, and spectral analysis was performed as well, using a FFT procedure.

2.2 Reynolds stress

Three different ways of calculating the Reynolds stresses (or rather the u-v product) were employed, each describing a different aspect of these stresses:

a) The Reynolds stress by its definition, from the original time dependent velocity vectors:

$$\tau(X, Y) = - \rho \overline{u(X, Y, t) * v(X, Y, t)}$$

where $u(X, Y, t) = U(X, Y, t) - \overline{U(X, Y)}$ and $v(X, Y, t) = V(X, Y, t) - \overline{V(X, Y)}$

b) The phase-locked averaged u-v product, producing a value containing the influence of all frequencies present at the phase-locked averaged velocity components' vectors (frequencies higher than the phase-locking frequency that were not filtered out during the phase-locked averaging process):

$$\langle \tau(x_0, y_0) \rangle = - \int_0^T \overline{U(x_0, y_0, t) \cdot V(x_0, y_0, t)} dt \quad 0 < t < T$$

where T is the time-period of the phase-locking frequency.

c) The Reynolds stress spectrum.

In order to obtain both the power spectra and the Reynolds stress spectra, we have used a fast Fourier transform operator (FFT). The result was a vector containing both the real and imaginary coefficients of various frequencies, for each velocity component.

$$\mathcal{L}(U) = C_1(\omega) \quad \text{where} \quad C_1(j) = A_1(j) + iB_1(j)$$

$$\mathcal{L}(V) = C_2(\omega) \quad \text{where} \quad C_2(j) = A_2(j) + iB_2(j)$$

where A(j) and B(j) are the sine's and the cosine's coefficients of the jth frequency, respectively. The sampling frequency (2.048 KHz), and the length of each channel's sampling vector (512 points), define both the lowest frequency, and the spectra's resolution to be 4 Hz, and the highest frequency to be 1.024 KHz.

The power spectra was calculated by multiplying the coefficients' vector $C_1(\omega)$ by its complex conjugate $C_1^*(\omega)$;

$$S_1(\omega) = C_1(\omega) \cdot C_1^*(\omega) \quad \text{where} \quad S_1(j) = A_1(j)^2 + B_1(j)^2$$

The Reynolds stress spectra was achieved by calculating the real part of the product of one velocity components' vector by the other's complex conjugate :

$$T(\omega) = 0.5 \text{ REAL}[C_1(\omega) * C_2^*(\omega)]$$

where $T(j) = -0.5[A_1(j) * A_2(j) + B_1(j) * B_2(j)]$.

2.3 Vorticity field

The phase-locked averaged vorticity field was computed by numerical differentiation of the phase-locked averaged velocity vectors.

The resulting phase-locked averaged vorticity signal $\langle w(X,Y,T) \rangle$ was used, both for plotting the iso-dynes (iso-vorticity contours), and for further mathematical operations (i.e. Fourier transformation in the disturbance frequency in order to obtain the vorticity eigenfunctions and compare them with the results of the stability theory).

2.4 Streaklines

A streakline connects, by definition, all fluid particles that have passed through a fixed point in space (a source point), during a given period of time.

In order to establish and draw a streakline from the velocity vectors, given in the Eulerian representation, one must transfer it to the Lagrangian

an representation , i.e. calculate the particles' pathlines given by:

$$r = r(R,t)$$

where R is the position vector of the particle at $t=0$.

Providing the Jacobyan of the equations' matrix has a non-zero value the following relation can be written:

$$R=R(r,t)$$

A streakline at a given time t^* can be directly calculated by the following expression:

$$r = r[R(r_0,t_0),t^*]$$

where r_0 is the position vector of a source point, t^* is a parameter defining the time at which the streakline is to be plotted and t_0 is the time variable $0 < t_0 < t^*$.

Another way of representing a pathline in a two-dimensional flow field , is:

$$U=dX/dt \quad ; \quad V=dY/dt \quad \text{with } X(t=t_0)=X_0 \quad \text{and } Y(t=t_0)=Y_0$$

where (X_0, Y_0) are the space coordinates of a source-point.

We restricted our discussion to a row of source-points, displaced vertically at the first X-station ($X=200$ mm). Thus we can represent the pathlines as :

$$r_1 = r_1(R,t_0,t)$$

where R is the source-points' position vector parameter, t_0 is the intial time parameter and t is the time variable. As the flow field considered is periodic, with a time-period T , it follows that:

$$r_1(R, t_0, t) = r_1(R, t_0 + nT, t) \quad n=1, 2, \dots$$

The pathlines were calculated by numerical integration of the phased-locked averaged velocity vectors.

Each source point (X_0, Y_0) produced NPP pathlines—the number of data points in the phase-locked averaged velocity vector. The pathline vectors were identified by an index j defined as $j=1+t_0/\Delta t$ where t_0 is the time the particle passed through the source point and Δt is the time interval between data points.

Since Δt is determined by the sampling frequency ($\Delta t=1/f$), the integration led us to space coordinates other than our measuring stations. Interpolation techniques were employed in order to establish the velocity values at those points. A spline interpolation procedure was first used in the transverse direction (Y-axis), and a linear interpolation method was then applied in the stream-wise direction (X-axis). Since the time-period corresponds to NPP data points, all time considerations reduce to a proper indexing of the points in the phase-locked averaged velocity vectors.

The function r_1 describes the position of all particles that had passed through a source point. Writing :

$$r_1 = r_1(R, t_0, t^*)$$

where R and t^* are now the parameters of the source point position and the plotting time respectively, and t_0 is the variable, ($0 < t_0 < t^*$), we represent the desired streaklines. The periodic flow field demands that:

$$r_1(R, t_0, t^*) = r_1(R, t_0, t^* + nT) \quad n=1, 2, \dots$$

Thus the streaklines' computation reduces to a proper picking-up procedure of data points from the pathlines' vectors.

If, for example, the streakline at the time corresponding to the i^{th} point of the phase-locked averaged vector is to be plotted (i.e. $t^* = i^* t$), the following points are to be picked up from the pathline vector indexed $j=1$:

$$i^{\text{th}}, NPP+i^{\text{th}}, 2*NPP+i^{\text{th}}, \dots, n*NPP+i^{\text{th}},$$

from the pathline indexed $j=2$ the following points are to be picked-up:

$$(i-1)^{\text{th}}, (NPP+i-1)^{\text{th}}, (2*NPP+i-1)^{\text{th}}, \dots, (n*NPP+i-1)^{\text{th}},$$

from the pathline indexed $j=j$ the following points are to be picked-up:

$$(i-j+1)^{\text{th}}, (NPP+i-j+1)^{\text{th}}, (2*NPP+i-j+1)^{\text{th}}, \dots, (n*NPP+i-j+1)^{\text{th}},$$

and from the pathline indexed $j=i$:

$$1^{\text{st}}, NPP^{\text{th}}, 2*NPP^{\text{th}}, \dots, n*NPP^{\text{th}},$$

etc.

The interval of NPP points between each two points picked up from the same pathline corresponds to the time period (T) of the flow.

Chapter 3

The Disturbed Mixing-Layer

3.1 Streaklines

One of the main objectives of this work was to compare the streaklines computed from experimentally measured velocity signals with conventional flow visualization pictures, thus providing a link between the qualitative observations of flow (flow visualization) and quantitative measurements taking into account the dynamics of the flow.

A collection of streaklines, each one originating from a different source-point, all displaced vertically at the first measuring-station ($X=200$ mm), are shown in Fig. 1. A comparison between this streaklines' pattern and a smoke picture is presented in Fig. 2, and the resemblance between the two is clearly seen. The smoke pictures were taken using stroboscopic illumination at the disturbance frequency, thus it represents a "phase-locked" averaged picture of 36 events.

The three regions of growth described in our first report, and shown in Fig. 3, can now be discussed in terms of the streaklines. Region I, which is marked by a rapid growth of the shear layer, can be characterized by amplification of disturbances in the lateral direction. Its length is therefore equal to the distance required for the vortex sheet to start rolling up into lumps. We define a lump as a structure in which the streak-

lines fold over backwards. The lateral dimension of the vortex lumps in region II remains unchanged while their inclination to the flow axis is being altered. The thin vortex sheet which separates adjacent lumps, and sometimes is referred to as the "braid", is stretched in the process. In region III the vortex lumps are leaning downstream on the high velocity side of the shear layer; their inclination angle to the axis of the flow continuously decreases with increasing distance from the splitter plate. The elongation of the vortex lumps and the change in their inclination angle causes one vortex lump to overlap another. The increase of the average momentum thickness in region I is concurrent with an increase in the lateral displacement amplitude of a streakline originating at the heart of the mixing-layer, which can be regarded as an interface separating the two mean streams. In region III the duration of passage of each vortical structure at a given station increases without a concomitant increase of its lateral dimension. This increase is responsible for the widening of the momentum thickness. In region II the inclination of the interface between the two streams is the greatest (crossing $\pi/2$) reducing to a local minimum the duration of the interface crossing and therefore . Neither the phase-locked streaklines nor the smoke pictures which are locked in phase to the flap oscillations exhibit any pairing process, so often discussed in the literature.

We have compared streaklines calculated from velocity signals phase-locked to the disturbance frequency with velocity signals phase-locked to its first subharmonic, and the two showed no distinct difference. The the first subharmonic of the oscillations' frequency has

no influence on the phase-locked streaklines pattern.

Fig. 4 shows a sequence of streakline patterns plotted with an interval of $\pi/2$ between them. One can thus observe the time-development of the flow field, the changes in the inclination angles of the structures while moving from region I to region II, and the stretching of the structures in region III.

The streakline patterns calculated from the measured velocities give a true descriptive picture of the phase-locked flow and can be used in comparing flow visualization to measurements of dynamically significant quantities such as the vorticity field, the Reynolds stresses, and the power spectra.

3.2 Vorticity field

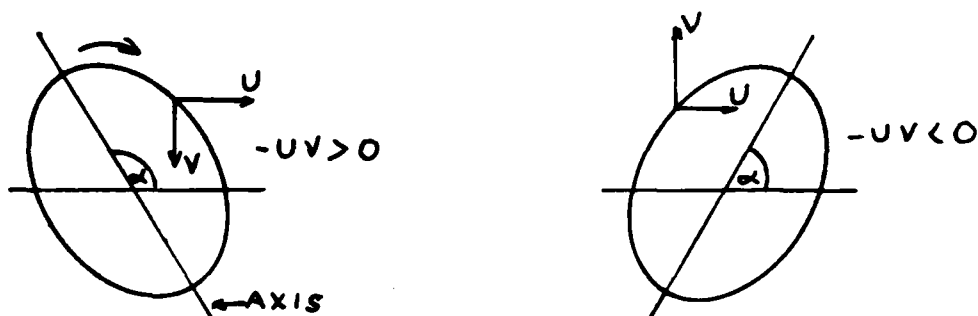
The isodynes (iso-vorticity contours) presented in Fig. 5 were calculated using the methods described in section 2.3, and they show the phase-locked vorticity field corresponding to the time (t^*) for which streaklines of Fig. 4 were drawn.

Each streakline structure concentrates excess vorticity in it and, therefore, may be loosely referred to as vortex. There are different distributions of vorticity in the three regions : A vortex in region I contains two cores, displaced both laterally and in the streamwise direction.

This description agrees with predictions based on linear stability theory as given by Michalke (1965). Each of the vortices seen in region II contains only one core. The vortices in region III are being stretched in the longitudinal direction, changing their shape from being approximately circular to being elliptical with an ever increasing major axis.

Fig. 6 shows a sequence of iso-vorticity contours plotted at $\pi/2$ interval between them, plotted at the same points as Fig. 4. The vorticity field, as well as the streaklines' pattern, is periodic, with a time period of T .

The inclination angle of a vortex is related to the sign of the Reynolds stress as schematically sketched below (Browand 1980). When the inclination angle of the eddy $\alpha > \pi/2$ the associated Reynolds stress is positive and when $\alpha < \pi/2$ the Reynolds stress changes sign, and becomes negative.



The phase-locked vortices in region I mapped by the isodynes or the streaklines, resemble ellipses with a negative inclination angle. It is expected that the phase-locked Reynolds stresses in this region would exhibit positive values, while the phase-locked Reynolds stresses of region II will go through zero and would be negative in region III, since the major

axes of the vortices in these regions have a positive inclination angle with the flow direction. The phase-locked Reynolds stresses are associated with the phase-locked energy production (see Hussain 1983) and it seems that while the phase-locked vortices of region I would extract energy from the mean flow (negative inclination angle, associated with positive phase-locked Reynolds stresses), they would lose energy to the mean flow in regions II and III. A more detailed discussion of the Reynolds stresses in the various flow regions is given in section 3.3.

The phase-locked vortices in region III show no increase in their lateral dimension while their longitudinal dimension increases (stretching process). This affects the mean width of the mixing-layer (or its momentum thickness) through the time integral of the velocity fluctuations that form the basis for the mean width. The longer the vortex, the greater its donation to the mean values.

3.3 Reynolds stress and power spectra

Since the Reynolds stress $= - u'v'$ is linked to the mean momentum equation, the changes in it must also reflect respective changes in the momentum thickness. Though the division of the flow field into three regions of different behaviour seems to fit at first sight, we have found that there are different characteristics of the flow within each of these regions, and we will discuss the Reynolds stress according to a more detailed division.

Profiles of the mean $-u'v'$ product (designated hereafter as $-uv$) at four characteristic stream-wise stations within the part of region I that exhibits linear growth of the mixing layer with increasing X , ($200 < X < 500$ mm), are plotted in Fig. 7, marked by crosses. The profiles are positive, implying that energy is transferred from the mean flow to fluctuations in the flow. On the same graph we have plotted profiles of the phase-locked $-u'v'$ product (designated hereafter as $\langle -uv \rangle$), marked by triangles. The two are essentially identical, both are positive, and the difference between the two is attributed to random turbulent fluctuations that have been filtered out by the phase-locked averaging. The mixing layer is dominated, in this region, by the phase-locked fluctuations that produce phase-locked kinetic energy by the action of the phase-locked averaged Reynolds stress against the mean strain rate U/Y .

In Fig. 8 the cross-spectra graphs at 4 lateral locations, in the same X -stations are plotted. The frequency range of each graph (and any spectral graph presented hereafter) is between 4 and 200 Hz, with a resolution of 4 Hz.

The dominant frequency in the cross spectra in this section of region I is the disturbance frequency, although the harmonic frequency is mostly detected, having a positive peak as well.

The power spectra graphs at the same locations are presented in Figs. 9 (The power spectra of the longitudinal component u) and 10 (the lateral component v). These graphs are plotted on semi-logarithmic coordinates, the

frequency axis being the same as the cross-spectra's, and the power axis divided into four orders of magnitude. The power spectra graphs reflect the dominance of the disturbance frequency and its higher harmonics. The region of linear momentum thickness growth is governed, therefore, by the phase-locked fluctuations of the disturbance frequency, to which energy is transferred.

In Fig 11 we have plotted two distributions: the crosses represent the local extramum of each $-uv$ profile, and the triangles the local extramum of the $\langle -uv \rangle$ profiles vs. the stream-wise coordinate X . These graphs emphasize the resemblance between the mean and phase-locked characteristics in this sub-region, and reflect the difference caused by turbulence.

The transition region between region I and II ($500 < X < 560$ mm) is characterized by the reduction of the mixing-layer's growth rate to 0 at $X=560$ mm. Fig. 12(a) represent profiles of the mean and phase-locked $-u'v'$ products at $X=520$ mm. A change in the sign of both profiles can be detected at the upper side of the profiles (faster stream side) and both are negative there. Fig. 13(a) shows the Reynolds stress spectra at the same X -location, and the disturbance frequency appearing there has a positive peak, whilst the first harmonic is negative at the faster-stream side and positive at the slower-stream side. At $X=560$ mm (Fig 12(b)) the maximum positive value of each profile at the faster-stream side is equal to the maximum negative value at the slower-stream side. At this location the first harmonic exhibits negative peaks all along the cross-section (Fig 13(b)), and the first negative peak appears at the faster-stream side at

the imposed frequency. The trend of the disturbance frequency to perform negative $-u'v'$ product values continues downstream to $X=640$ mm, where the last peak at the slower-stream side becomes negative. (Fig. 13(c) and (d)). This trend appears at both types of the $-u'v'$ profiles as a continuous transition of the values at the slower-stream side to become negative. The energy spectra of both velocity components (Figs. 14 and 15) at the same X -station still reflect the dominance of the oscillations frequency and its higher harmonics, over the flow.

The transition of the mixing-layer from a region of growth to a region of shrinking in size, involves an interaction between the mean flow and phase-locked fluctuations of both the disturbance frequency and its first harmonic. It seems that the reduction in the mixing-layer's growth-rate begins at a point where the first harmonic's component of the $-u'v'$ product changes sign, and becomes negative at the faster-stream side. The fluctuations at this frequency lose energy to the mean flow, whilst the phase-locked fluctuations at the imposed frequency are still extracting energy from it (characterized by positive peaks at the cross-spectra graphs). The balance between the two across the flow determines the rate of growth of the mixing-layer. At stations where the components of the oscillations frequency are positive and higher than the negative values of the first harmonic components ($500 < X < 560$ mm), the phase-locked profile is partly positive and partly negative and the positive values are higher than the negative absolute values. The integral of the profile over the cross-section is consequently positive, causing the mixing layer to grow at a slower rate than at earlier stages of region I. At $X=560$ mm, where the

the imposed frequency turns negative too, there is some equilibrium between the positive phase-locked behaviour at the faster-stream side and the negative behaviour at the slower-stream side causing an inhibition in the mixing-layer's growth. During the transition of the imposed oscillations frequency toward negative values, the phase-locked profiles also become negative, and since the phase-locked phenomena governs the flow as reflected by the resemblance between the two types of profiles in this sub-region, it causes an energy transfer from the phase-locked fluctuations to the mean flow, followed by a reduction in the mixing layer's width.

Thus, instead of dividing the mixing layer into a region of growth (region I) and a region of shrinking (region II) we have divided it to a region of linear growth ($X < 500$ mm), a transition region ($500 < X < 640$ mm), and a region of shrinking that will be discussed below. The transition region is characterized by a gradual change of the growth rate from the constant value of the linear region to the negative value of the shrinking region.

The region of decreasing momentum thickness ($640 < X < 840$ mm) is characterized by negative profiles of both $-uv$ and $\langle -uv \rangle$ (Fig. 16). The absolute value of each minimum reduces with increasing X , the value of the mean minimum decreases faster than the phase-locked. The first mean positive extremum appears at $X=840$ mm. The difference between the two types of profiles increases with increasing X and is attributed to non-locked fluctuations at frequencies lower than the imposed frequency that appear in the flow and are seen at the cross-spectra, u -power spectra and v -power

spectra graphs (Figs. 17, 18 and 19, respectively).

The negative values of the $-uv$ profiles in this region are in accordance with the shrinking of the momentum thickness, most of the energy lost to the mean flow is due to the phase-locked frequencies (the disturbance frequency and its first harmonic) exhibiting negative peaks at the cross-spectra graphs of Fig. 17 that cause the phase-locked $-u'v'$ profile to be negative all over, but fluctuations at lower frequencies that are not locked in phase with the imposed oscillations extract energy from the mean flow. Their contribution is still rather small.

$X=840$ mm is another point of change in the mixing layer's behaviour, and it marks the boundary between the region of shrinking mixing layer (region II) and the region of the regrowth of the mixing layer linearly with X (region III). But within region III we have found a second transition sub-region bounded between $840 < X < 1080$ mm.

This transition sub-region is characterized by positive values that appear at the phase-locked $-u'v'$ product profiles (Fig, 20). The mean $-uv$ profiles remain positive throughout this region and downstream, and are in accordance with the growth of the mixing-layer. The phase-locked positive values imply that part of the large eddies (their center) is gaining energy from the mean flow, while other parts are losing energy. The important role of the positive values of the phase-locked profiles is demonstrated in Fig. 11 where the extrema of the $\langle -uv \rangle$ profiles appear to be positive in this region, between negative extrema up and downstream. This behaviour

can be explained in view of linear stability considerations that predict that whenever the momentum thickness of the mixing-layer is smaller than a given value (corresponding to the value of the neutral case) the layer is unstable to disturbances in the imposed frequency. Thus it is possible that the vortices of the oscillation's frequency are gaining energy due to the mixing layer's instability, up to a point where the momentum thickness reaches its saturation value ($X=1080$ mm). The first harmonic exhibits positive peaks at the Reynolds stress spectra starting at $X=860$ and downstream, its value decreasing with increasing X . The Reynolds stress spectra and the power spectra graphs (Figs. 21, 22 and 23) exhibit the dominance of the disturbance frequency, and the existence of non-phase-locked frequencies.

The rest of region III ($1080 < X$ mm) is characterized by the following features: The mean $-u'v'$ product profiles are all positive, and in accordance with the mixing-layer's growth (Fig. 24). The $\langle -uv \rangle$ profiles are negative and imply that the phase-locked vortices are losing energy to the turbulent mean flow. They do dominate the Reynolds stress spectra (Fig. 25), but other non phase-locked frequencies that exhibit lower peaks appear and are responsible for the mixing-layer's growth. It may be noted that the two distinct frequencies that appear in this region are 12 and 32 Hz. Nowhere along this region does the first subharmonic of the imposed frequency appear. Since this frequency is assumed to govern phase-locked eddy amalgamations, it is obvious that such a mechanism would not exist in this mixing-layer. The regrowth of the mixing-layer in region III can be attributed to either random amalgamations of vortices, or some non-linear inter-

action of fluctuations at the lower frequencies, that are not locked in phase with the disturbance. This conclusion is in agreement with the conclusion of Ho and Huang (1980), that the subharmonic is the agent rather than the product of the vortex amalgamations.

REFERENCES

- . ACTON, E.: 1976, J. Fluid Mech., 76, 651.

- . ASHURST, W.T.:
1976, Bulletin of the Amer. Phy. Soc., Ser. II, V.20,
1428.

- . BREIDENTHAL, R.: 1980, Phys. of Fluids, 23(10), 1929.

- . BROWAND, F.K. and TROUTT, T.: 1980, J. Fluid Mech. 97, 772.

- . BROWN, G.L. and ROSHKO, A.:
1971, Turbulent Shear Flows, AGARD-CP-93, 23-1.

- . BROWN, G.L. and ROSHKO, A.: 1974, J. Fluid Mech. 64, part 4, 775.

- . CHANDRSUDA, C., MEHTA, R.D., WEIR, A.D., and BRADSHAW, P.:
1978, J. Fluid Mech. 85, part 4, 693.

- . CORCOS, G.M. and SHERMAN, F.S.: 1976, J. Fluid Mech., 73, 241.

- . CRIGHTON, D.G. and GASTER, M.: 1976, J. Fluid Mech. 77, 397

- . DIMOTAKIS, P.E. and BROWN, G.L.:
1976, J. Fluid Mech. 78, part 3, 535.

- . GASTER, M., WYGNANSKI, I. and KIT, E:
Large Scale Structures in a Forced Turbulent Mixing Layer
(to be published in J. Fluid Mech.).

- . HO, C.M. and HUANG, L.S.:
1978, Bulletin of the Amer. Phys. Soc., Ser II., vol. 23,
1007.

- . HO, C.M. and HUANG, L.S.:
1982, J. Fluid Mech., 119, 443.

- . HUSSAIN, A.K.M.F.: 1983, Phys. Fluids 26, 2816

- . INOUE, O.: 1983, ISAS Research note 228.

- . MICHALKE, A.: 1964, J. Fluid Mech. 19, 543

- . MICHALKE, A.: 1965, J. Fluid Mech. 23, 521

- . MONKEWITZ, P.A. and HUERRE, P.:
1982, Phys. of Fluids, 25(7), 1137.

- . OSTER, D. and WYGNANSKI, I.: 1982, J. Fluid Mech. 123, 91

- . OSTER, D., WYGNANSKI, I., and FIEDLER, H.:
1977, Turbulence in Internal Flows, 67, hemisphere Press,

Washington, D.C.

- . PUI, N.K. and GARTSHORE, I.: 1979, J. Fluid Mech. 91, part 1, 111.
- . RILEY, J.J. and METCALFE, R.W.: 1980, AIAA Paper No. 80-0274.
- . ROSHKO, A.; 1976, AIAA Journal, 10, 1349.
- . WINANT, C.D. and BROWAND, F.K.:
1974, J. Fluid Mech. 63, part 2, 237.
- . WYGNANSKI, I., OSTER, D., FIEDLER, H. and DZIOMBA B.:
1979, J. Fluid Mech. 93, part 2, 325.

Figure Captions

Fig No.

1. Particle Streaklines.
2. Comparison between Calculated Streaklines and Smoke Picture.
3. Three Regions of the Mixing Layer.
4. Sequence of Streaklines.
5. Iso-Vorticity Contours.
6. Iso-Vorticity Contours.
7. Mean uv product.
8. Cross Spectra Distributions.
9. Power Spectra Distributions of U .
10. Power Spectra Distributions of V .
11. Distributions of $-uv$ and $\langle -uv \rangle$.
12. Mean and Phase Locked $-uv$ Products.
13. Reynolds Stress Spectra.
14. Energy Spectra of U .
15. Energy Spectra of V .
16. Momentum Thickness.
17. Cross Spectra.
18. U Power Spectra.
19. V Power Spectra.
20. Transition Sub Region.
21. Reynolds Stress Spectra.
22. U Power Spectra.

23. V Power Spectra.
24. Mixing Layer at Region III.
25. Reynolds Stress Spectra.

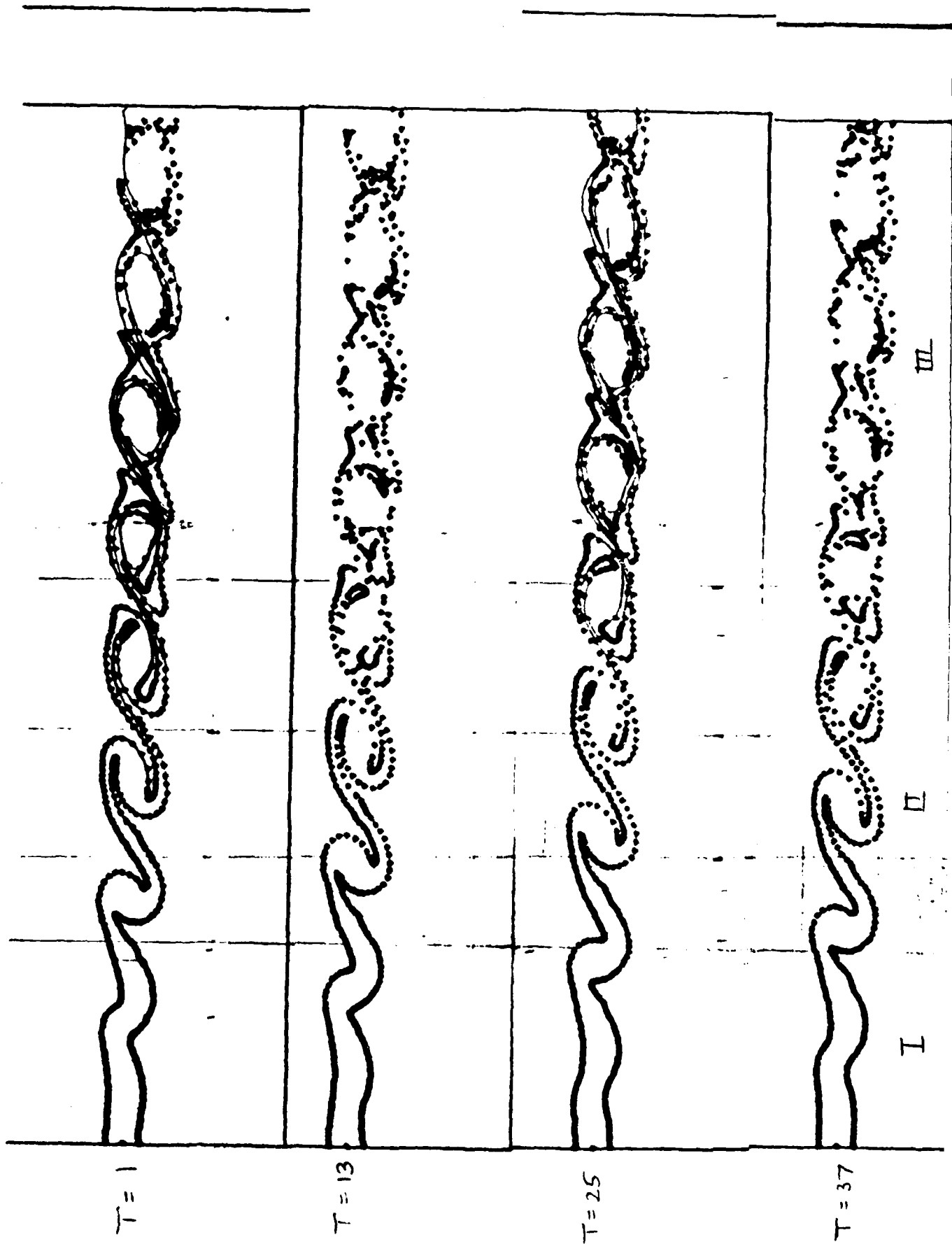


Fig. 1

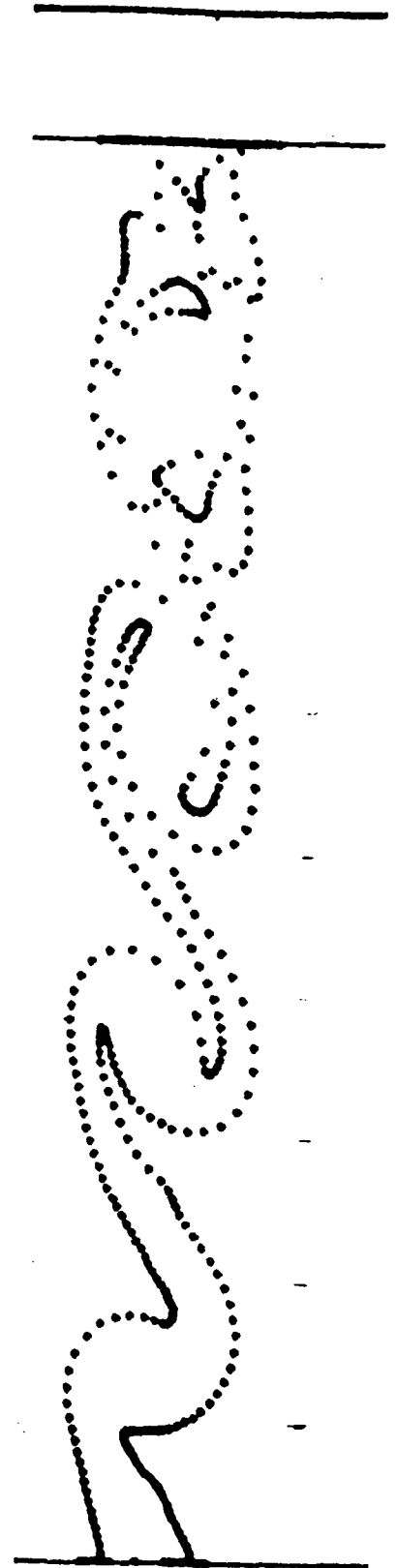


Fig.2

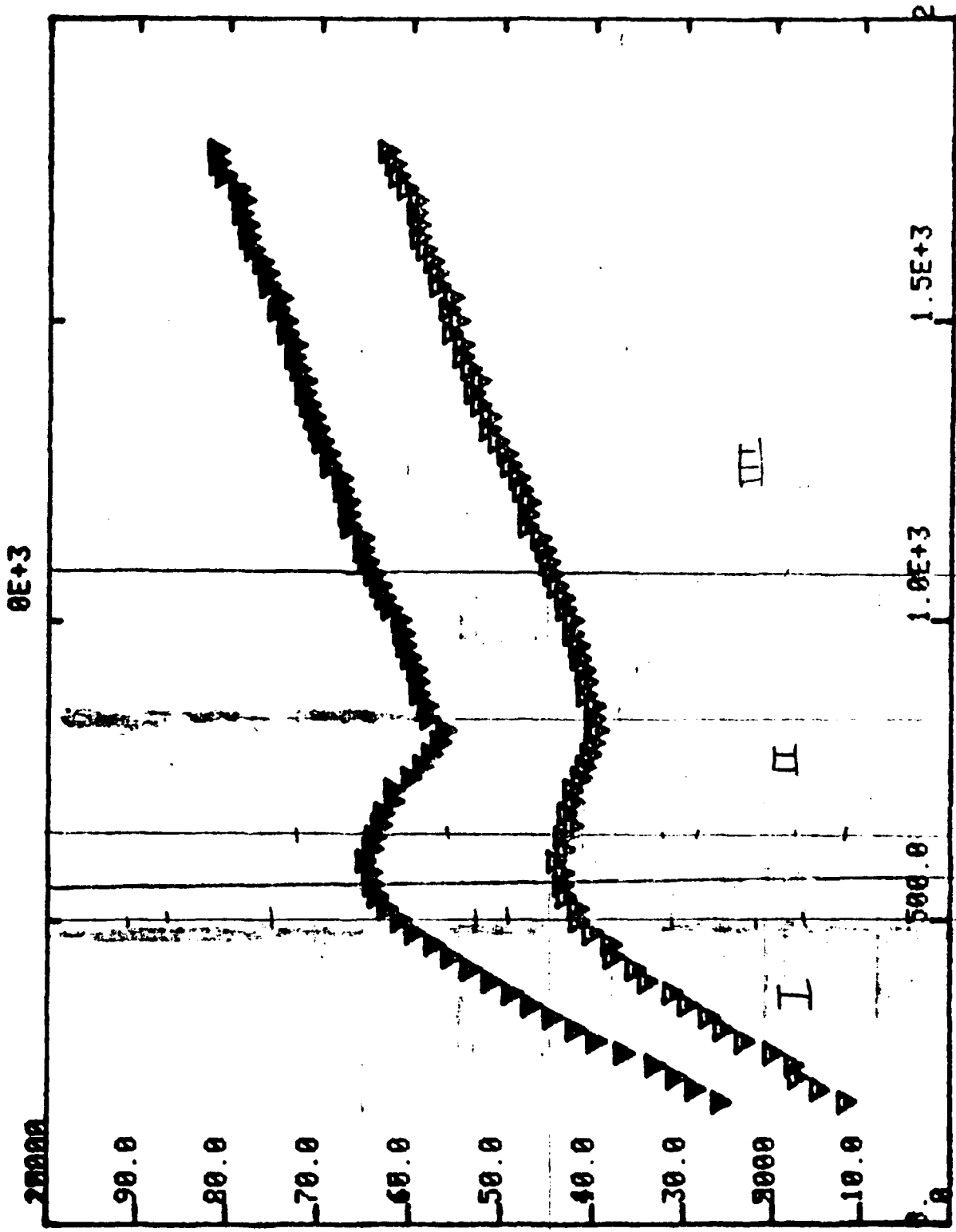


Fig. 3

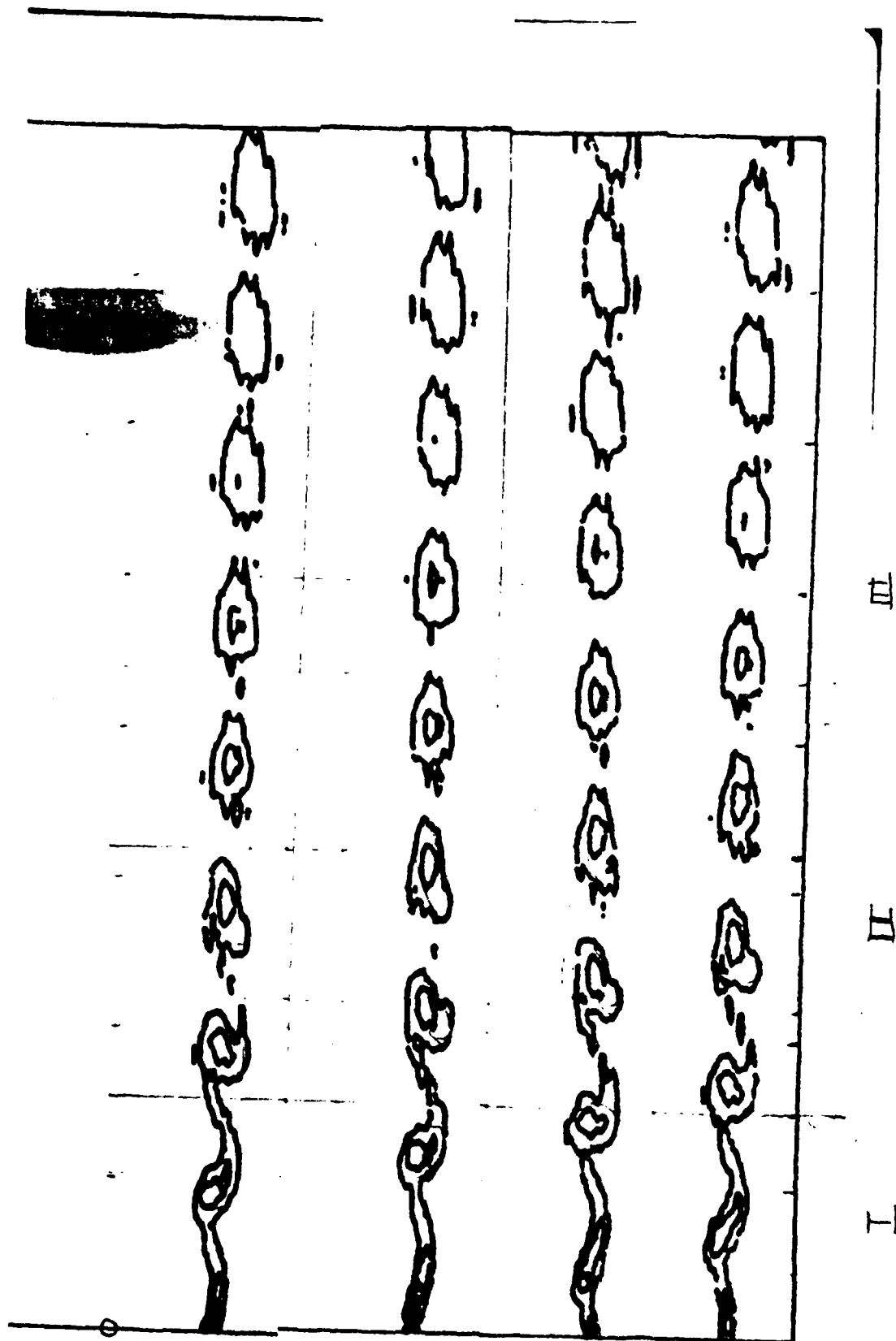


Fig. 4

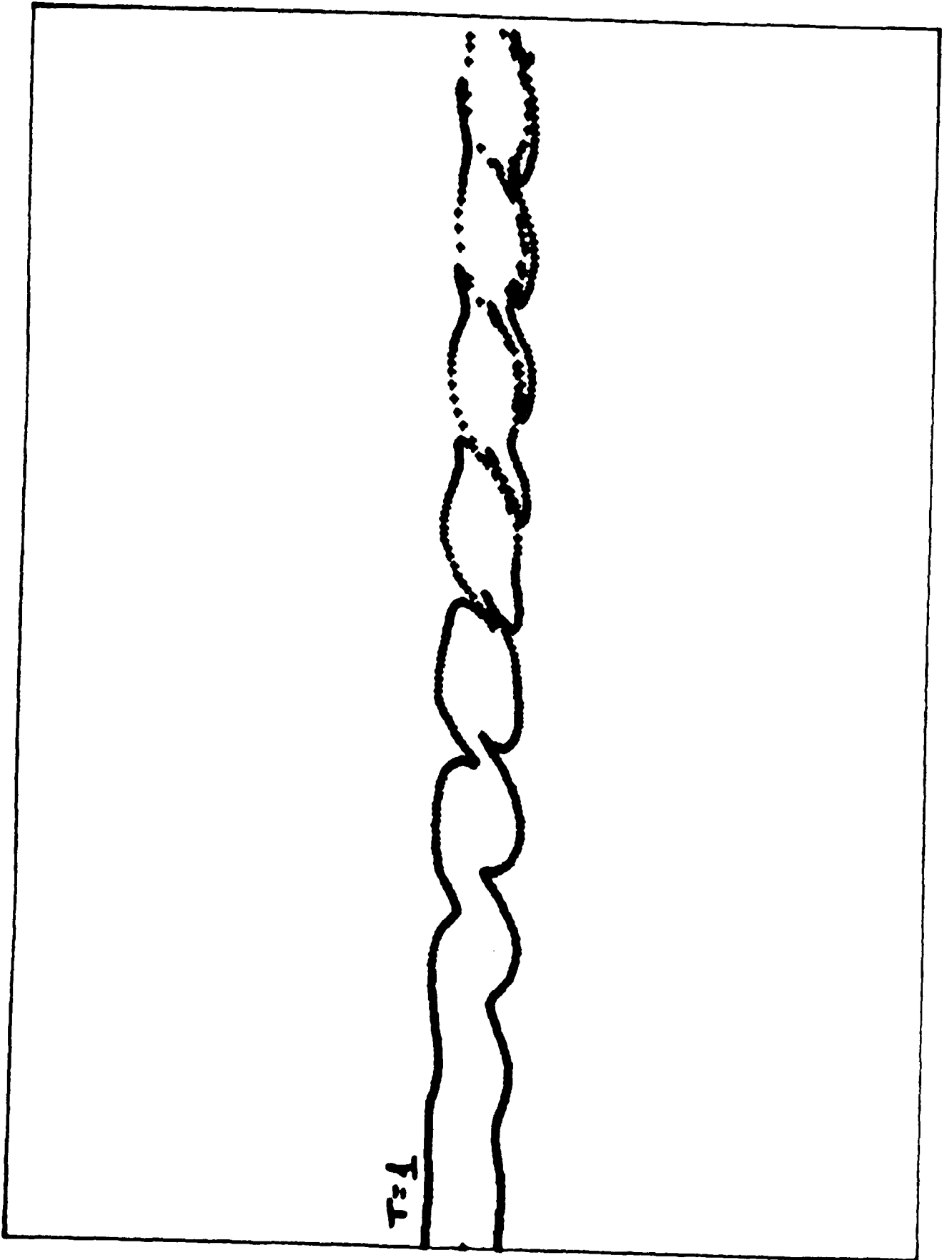


Fig. 5

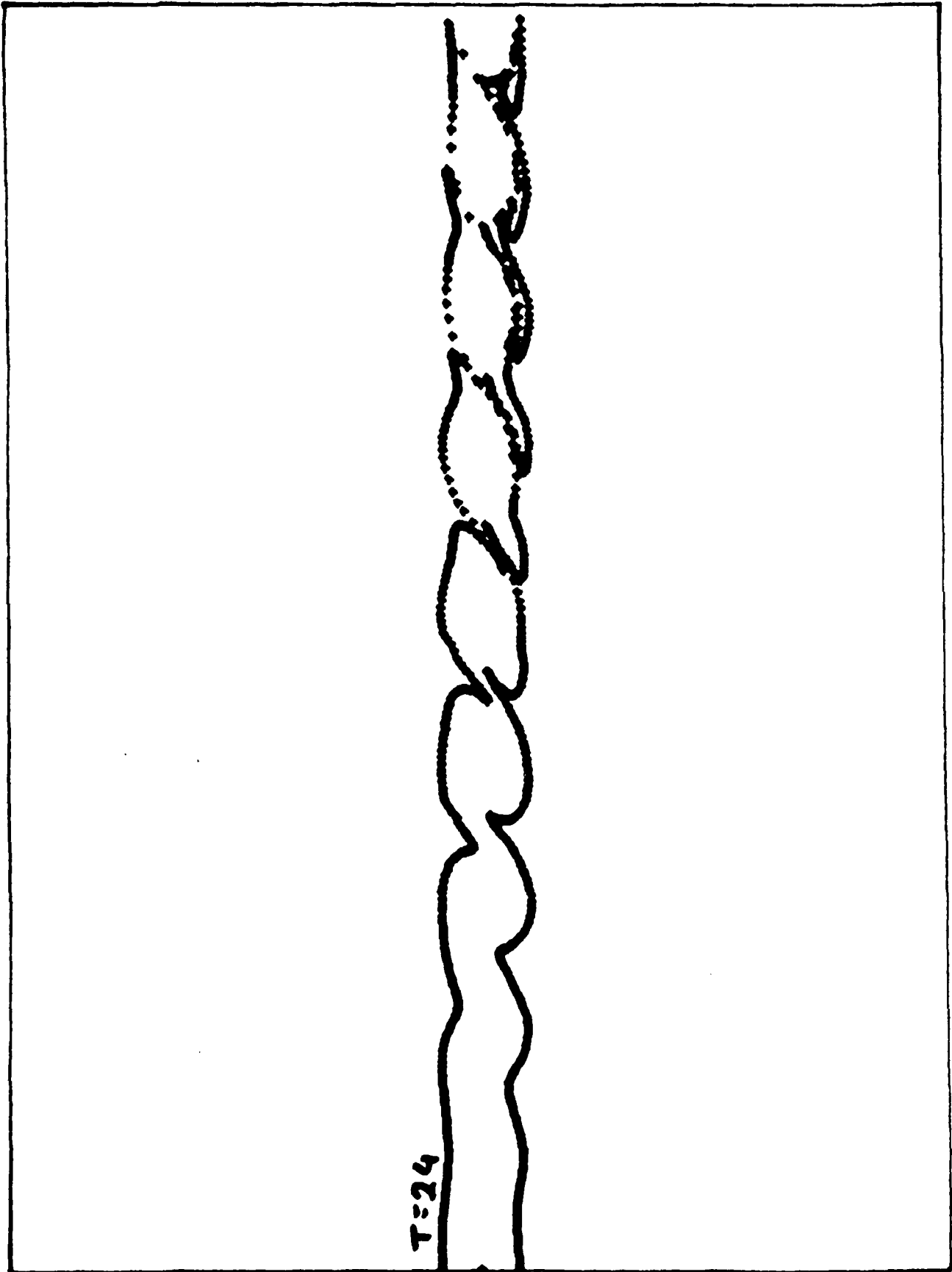


Fig. 6

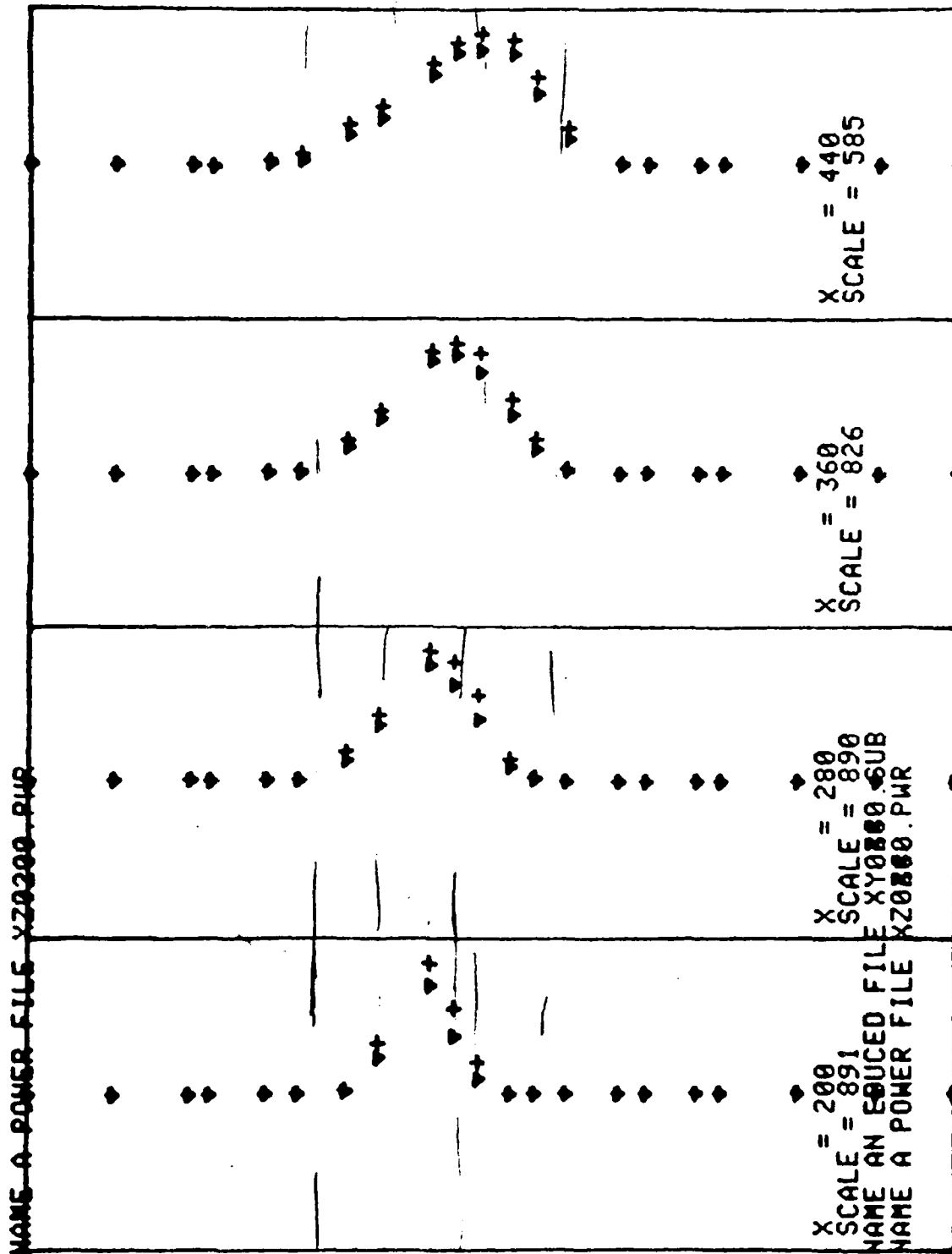


Fig. 7

NAME AN INPUT FILEXZ0300.PWR S(3) = -0.57724 S(4) = 0.86587

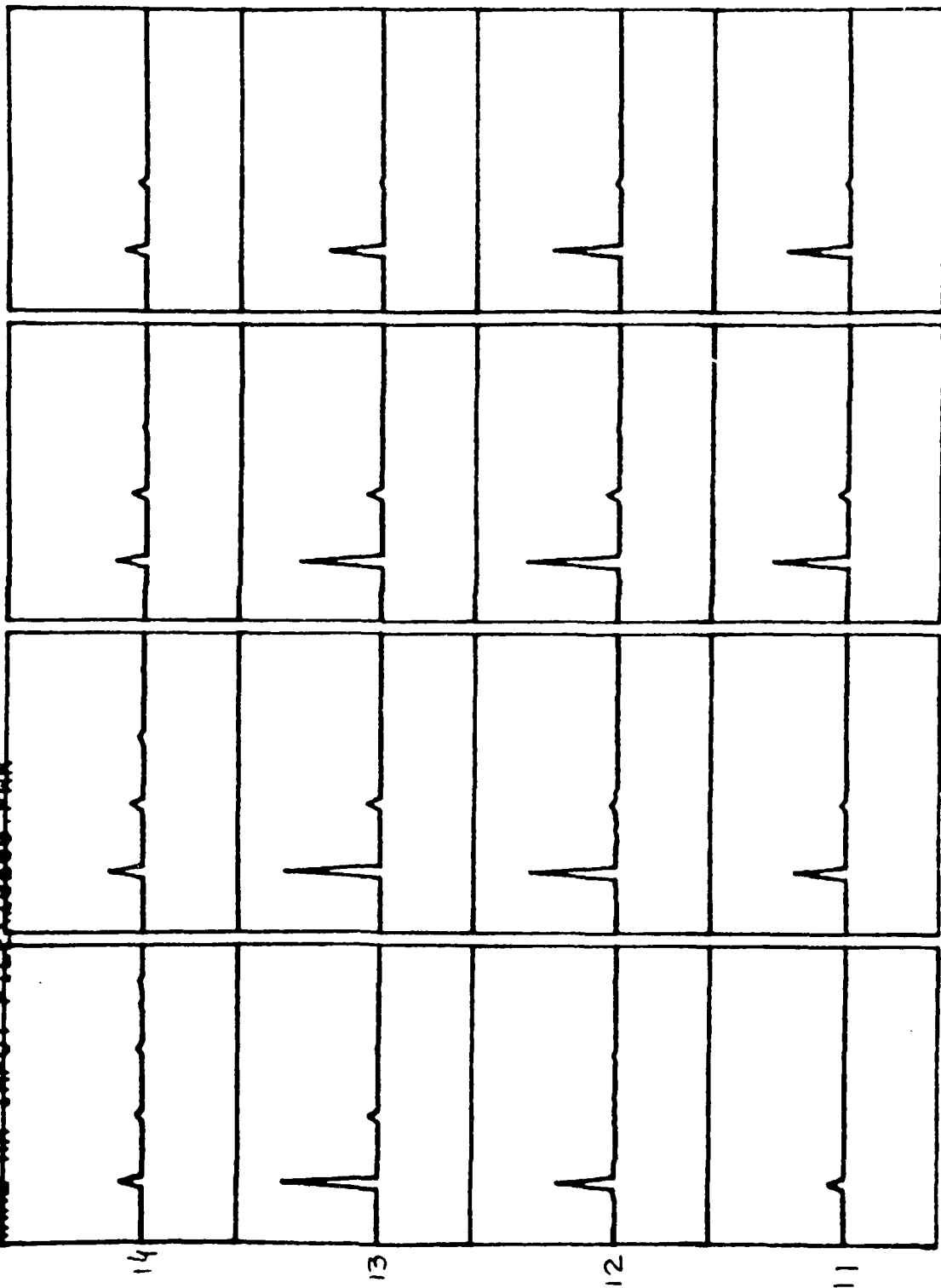


Fig. 8

S(3) = 0.23872E-3 S(4) = 2.86462

NAME AN INPUT FILE Y20200.PHR

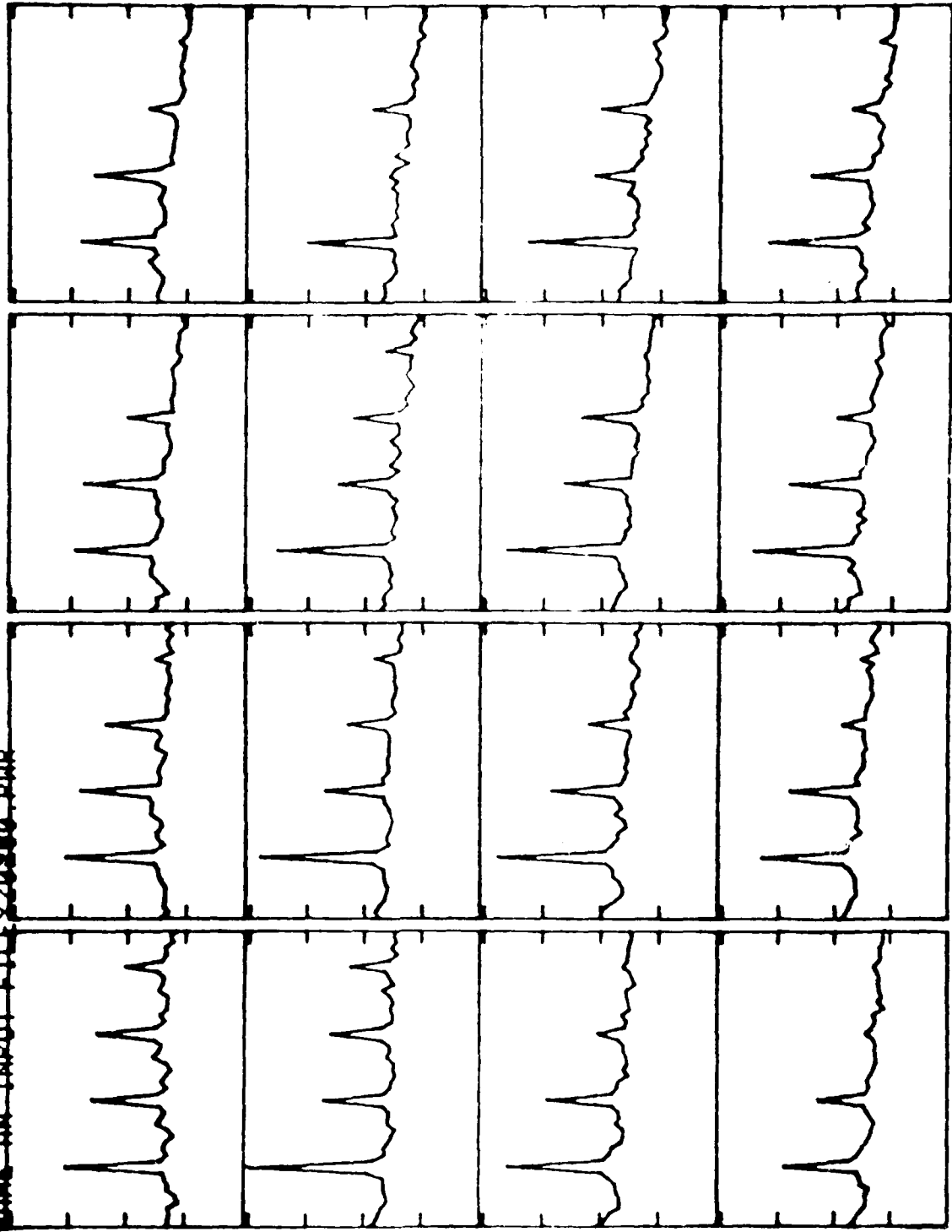


Fig. 9

NAME AN INPUT FILE YZ0360.PHR
 $S(3) = 0.57435E-4$ $S(4) = 0.68922$

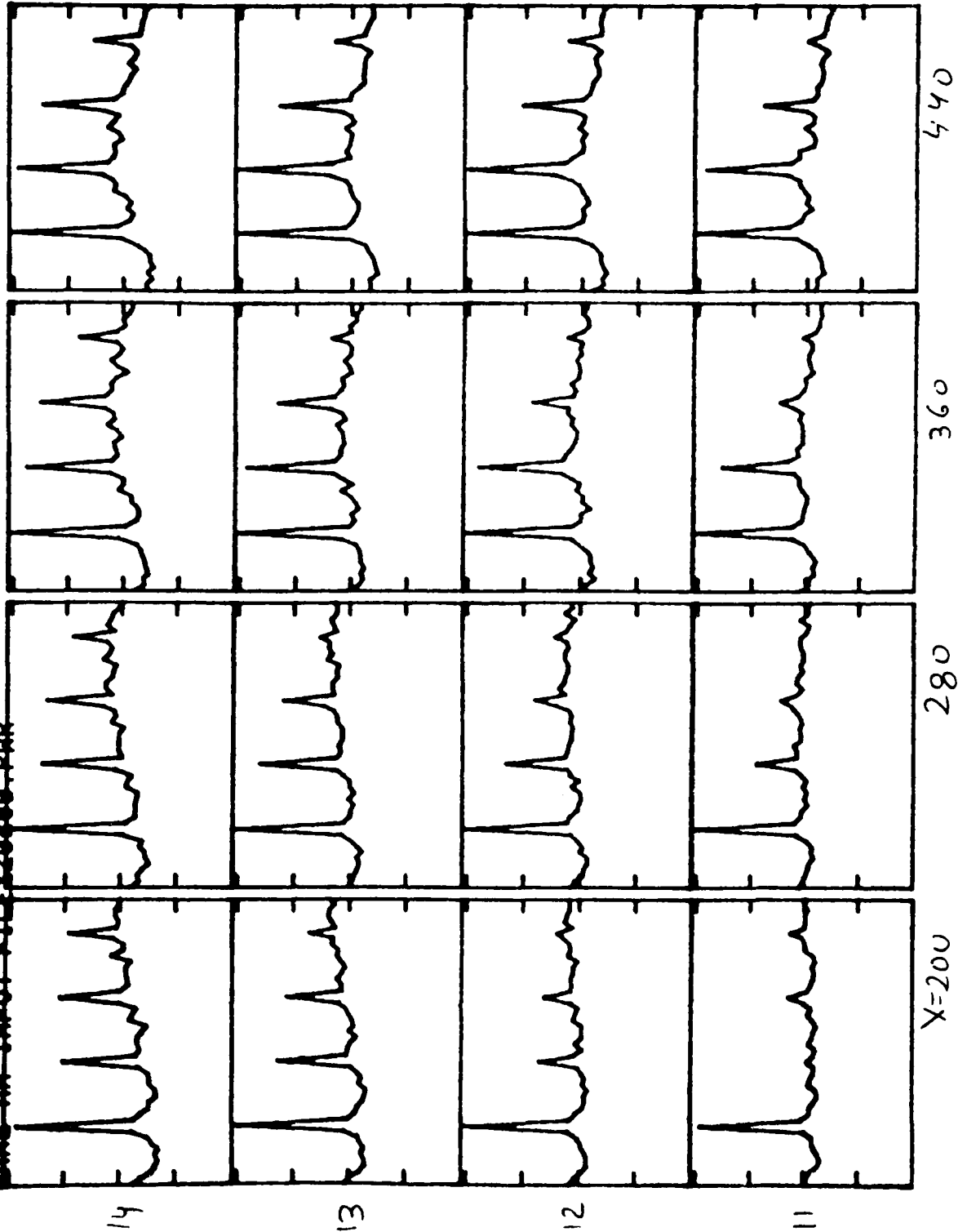
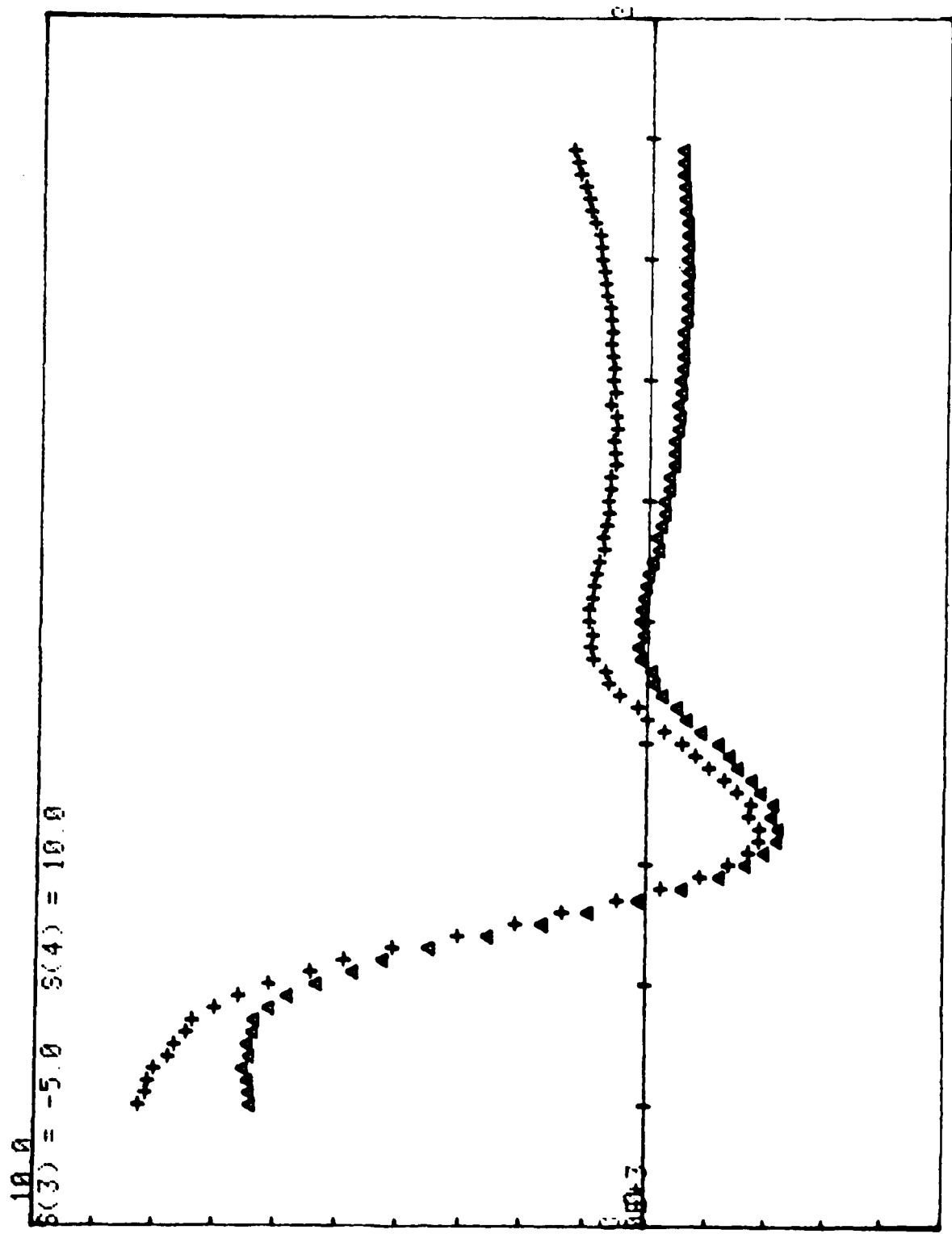


Fig. 10



10.0
 $S(3) = -5.0$ $S(4) = 10.0$

Fig. 11

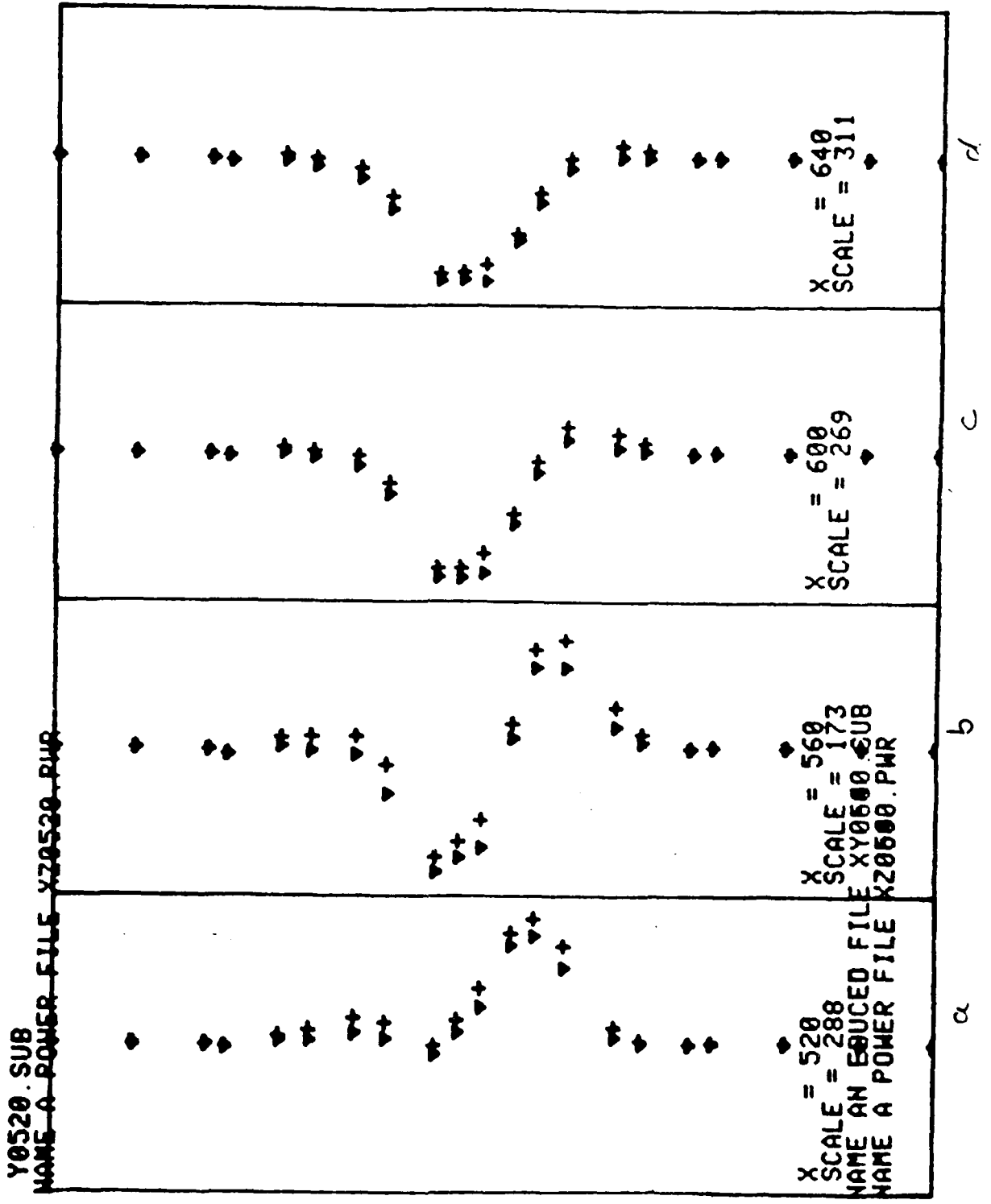


Fig. 12

NAME AN INPUT FILEXZ9550.PHR S(3) = -0.20576 S(4) = 0.30864



X = 520

560

600

640

Fig. 13

NAME=AN-INPUT-FILEXYZ000000.PUP S(3) = 0.49656E-4 S(4) = 0.59587

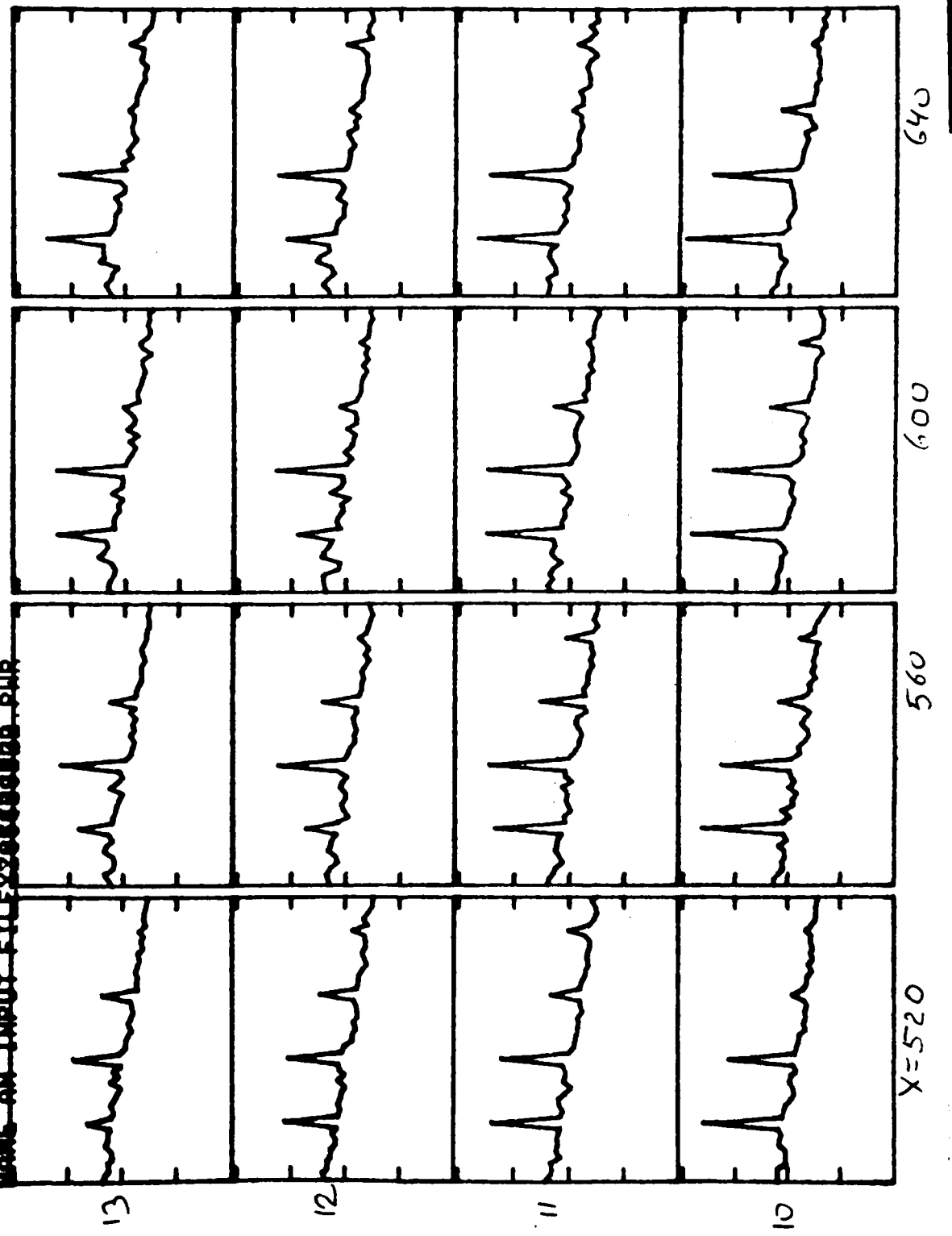


Fig. 14

NAME AN INPUT FILEYZ0880.PHR S(3) = 0.19654E-3 S(4) = 2.35848

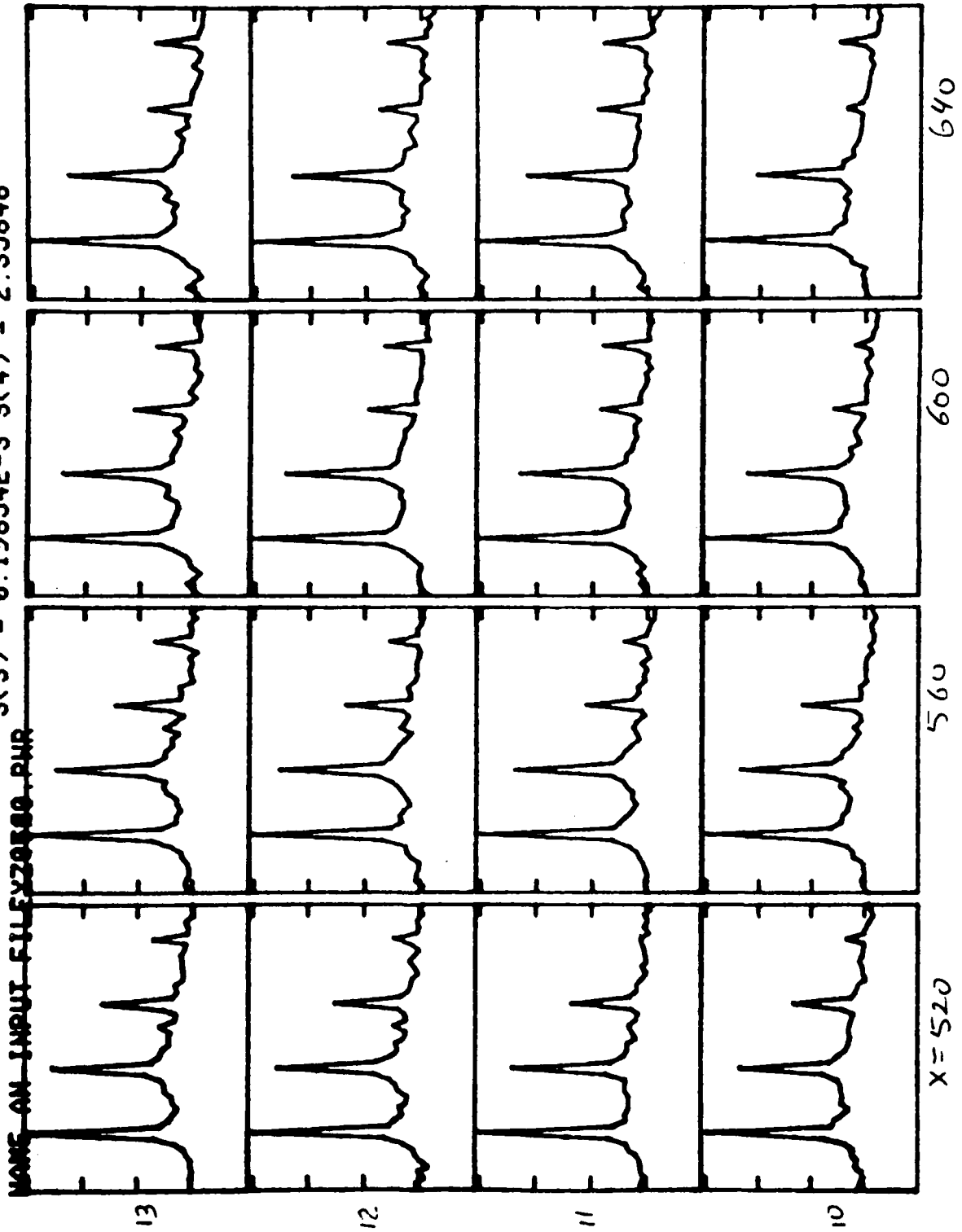


Fig. 15

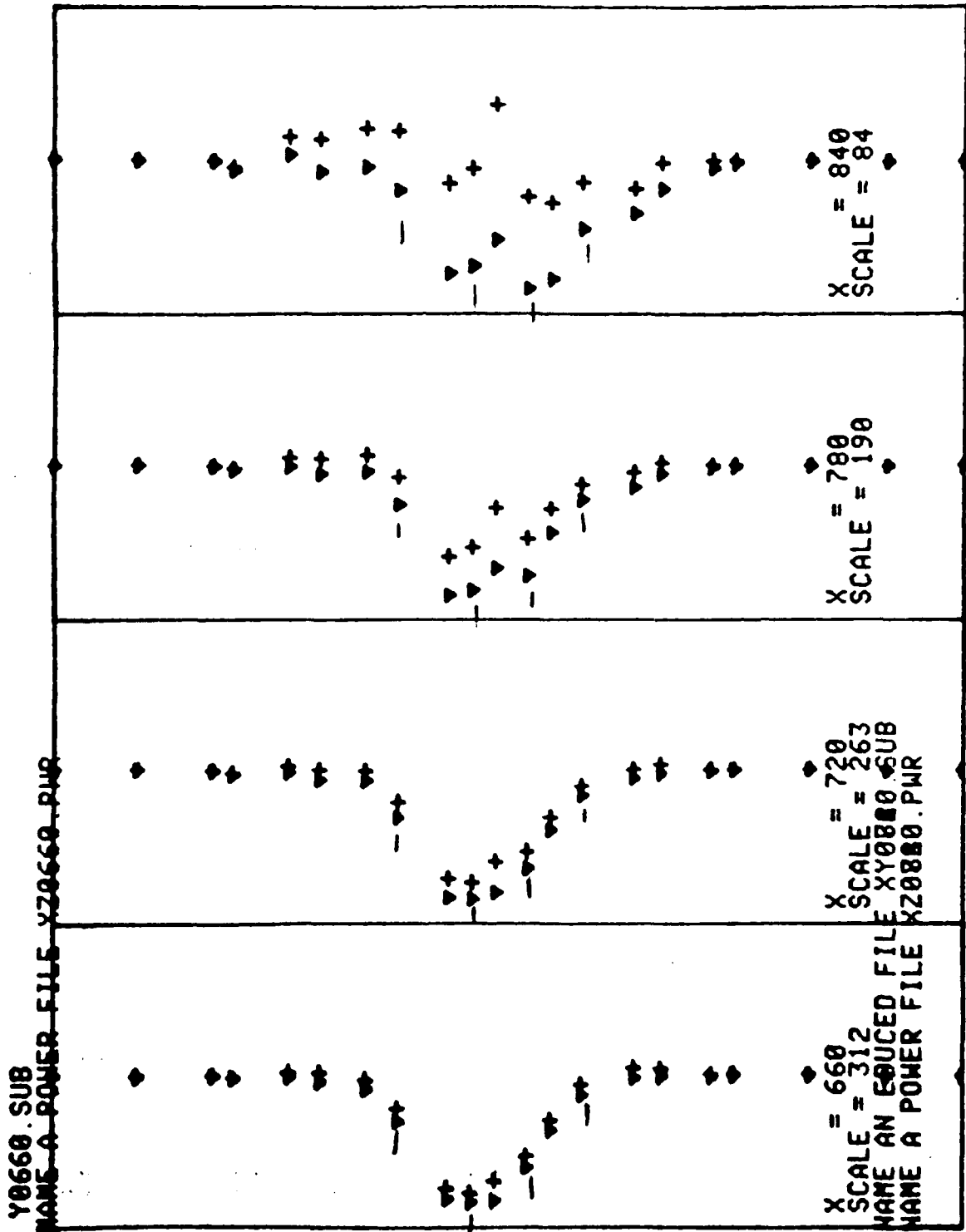


Fig. 16

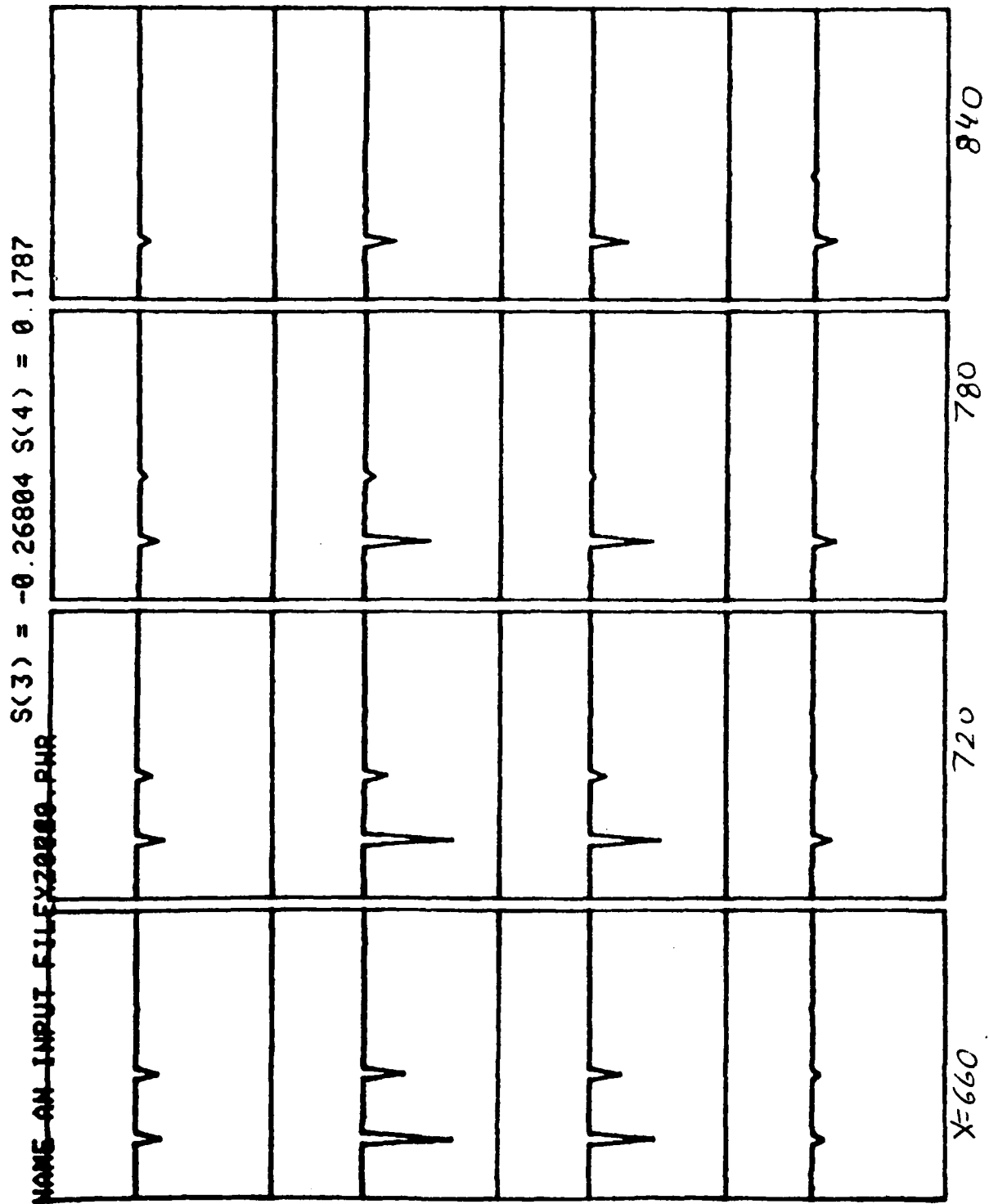


Fig. 17

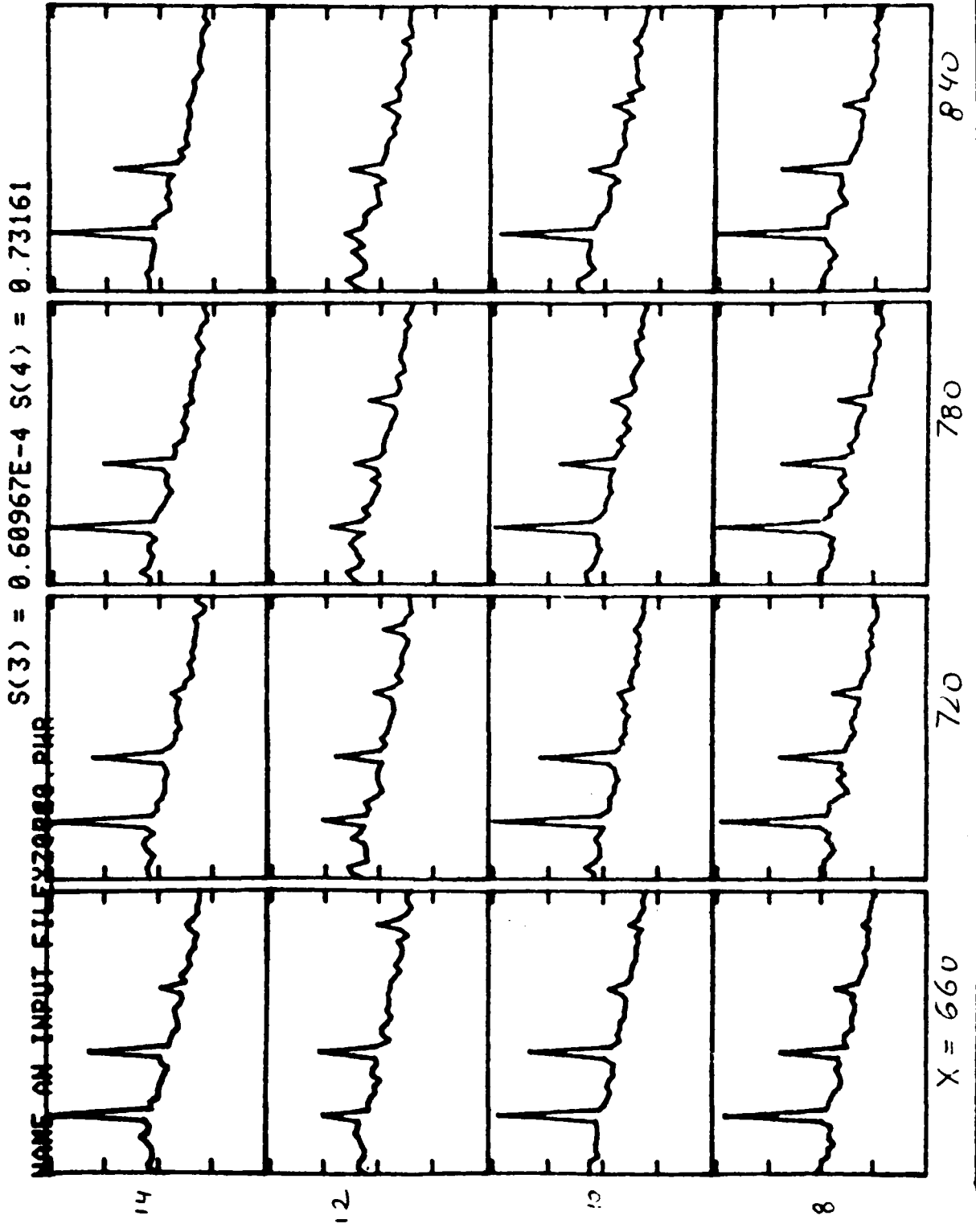


Fig. 18

NAME AN INPUT FILE Y20880.PHR S(3) = 0.23108E-3 S(4) = 2.773

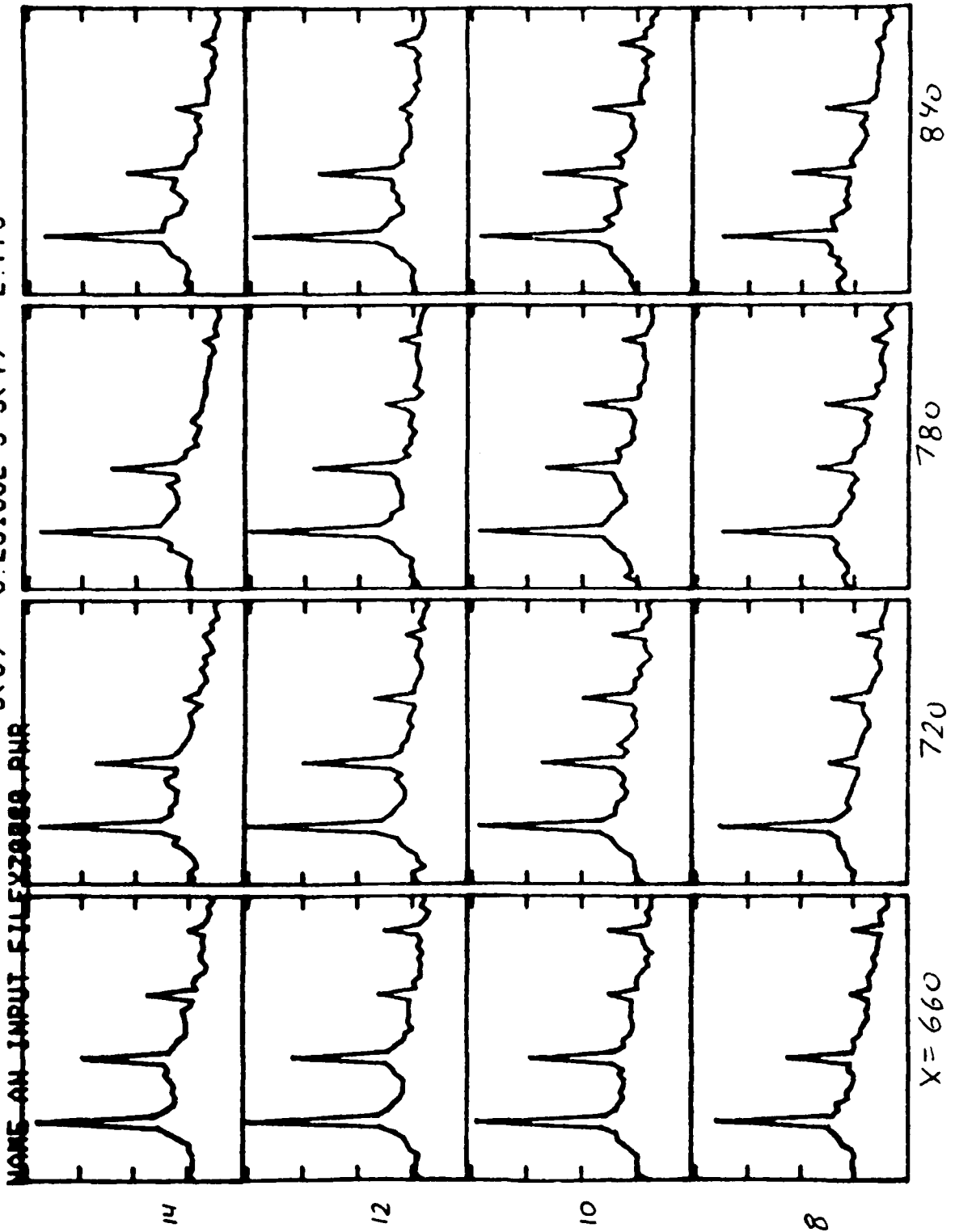


Fig. 19

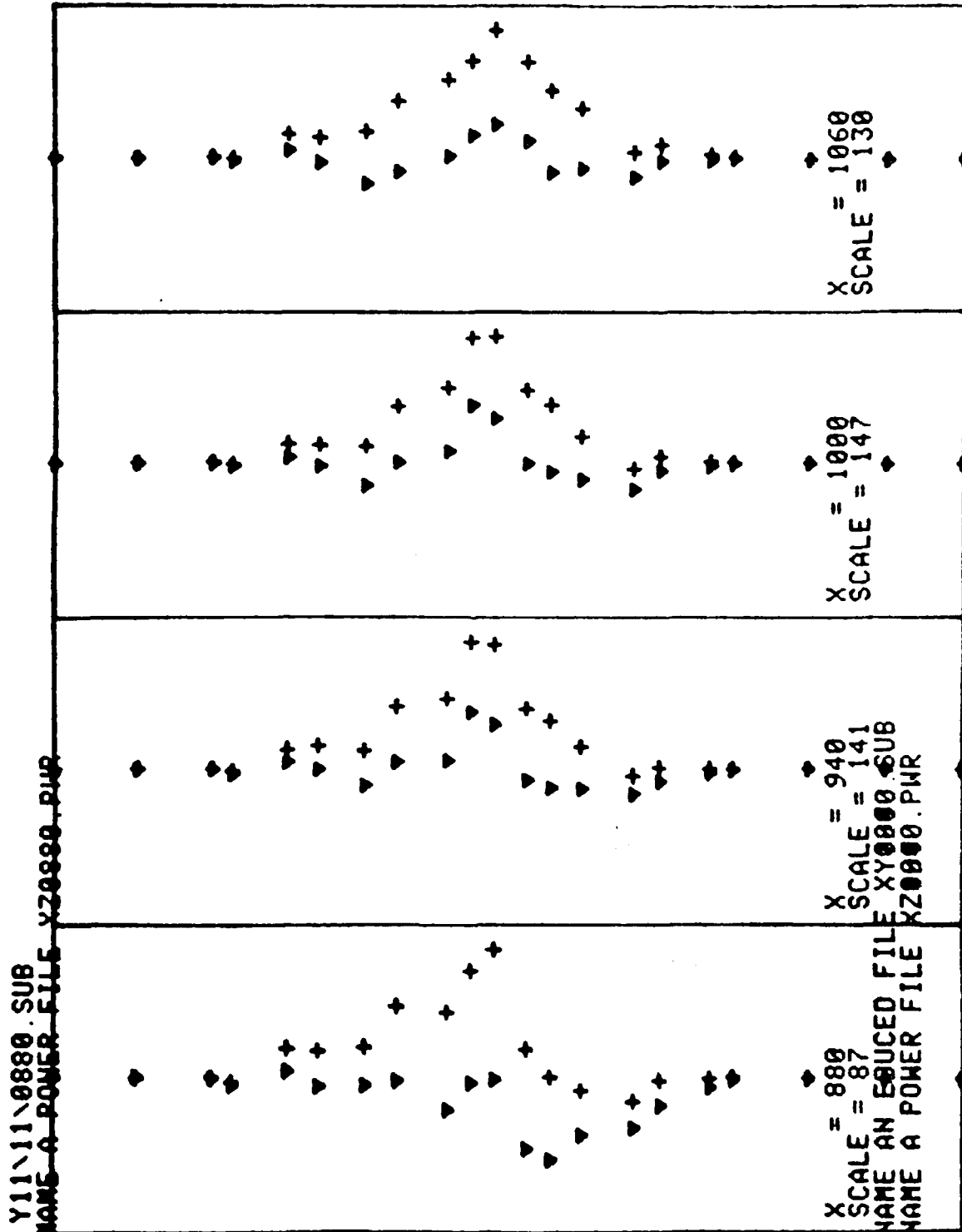


Fig. 20

S(3) = -0.72568E-1 S(4) = 0.48379E-1

NAME=AN INPUT FILEXZ0000.PHR

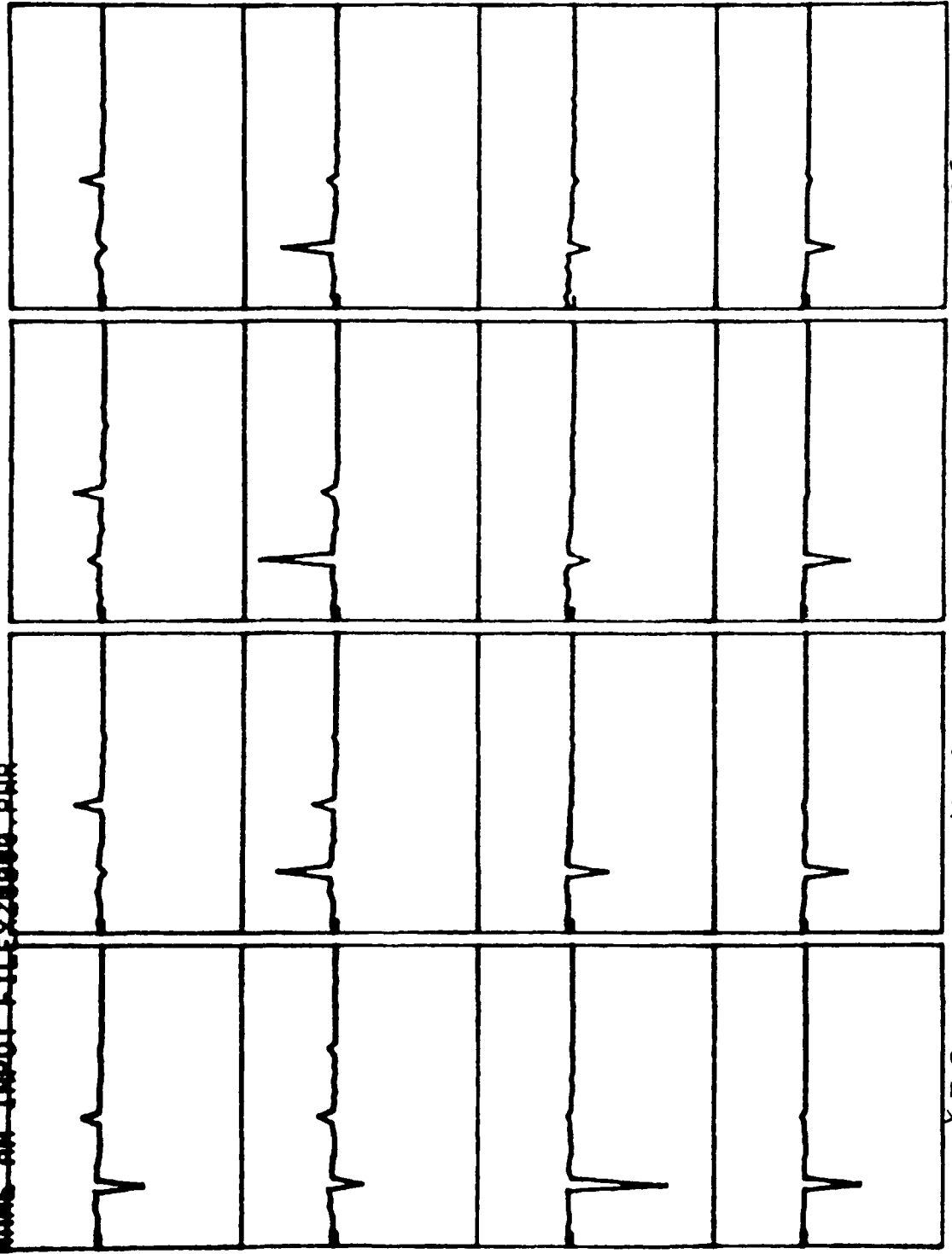


Fig. 21

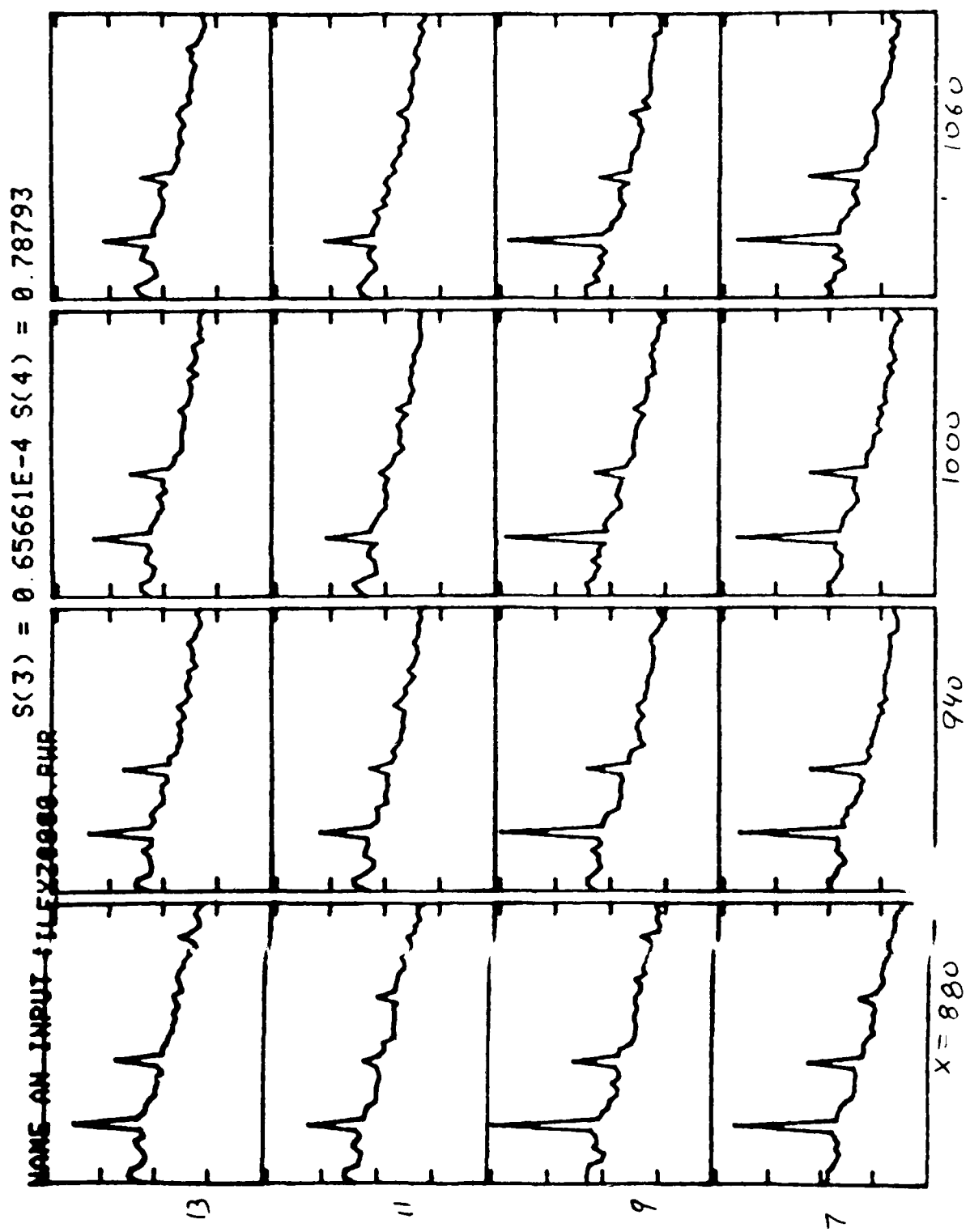


Fig. 22

ROWS ON INPUT FILEYZ0000.PPREFUP S(3) = 0.19219E-3 S(4) = 2.30627

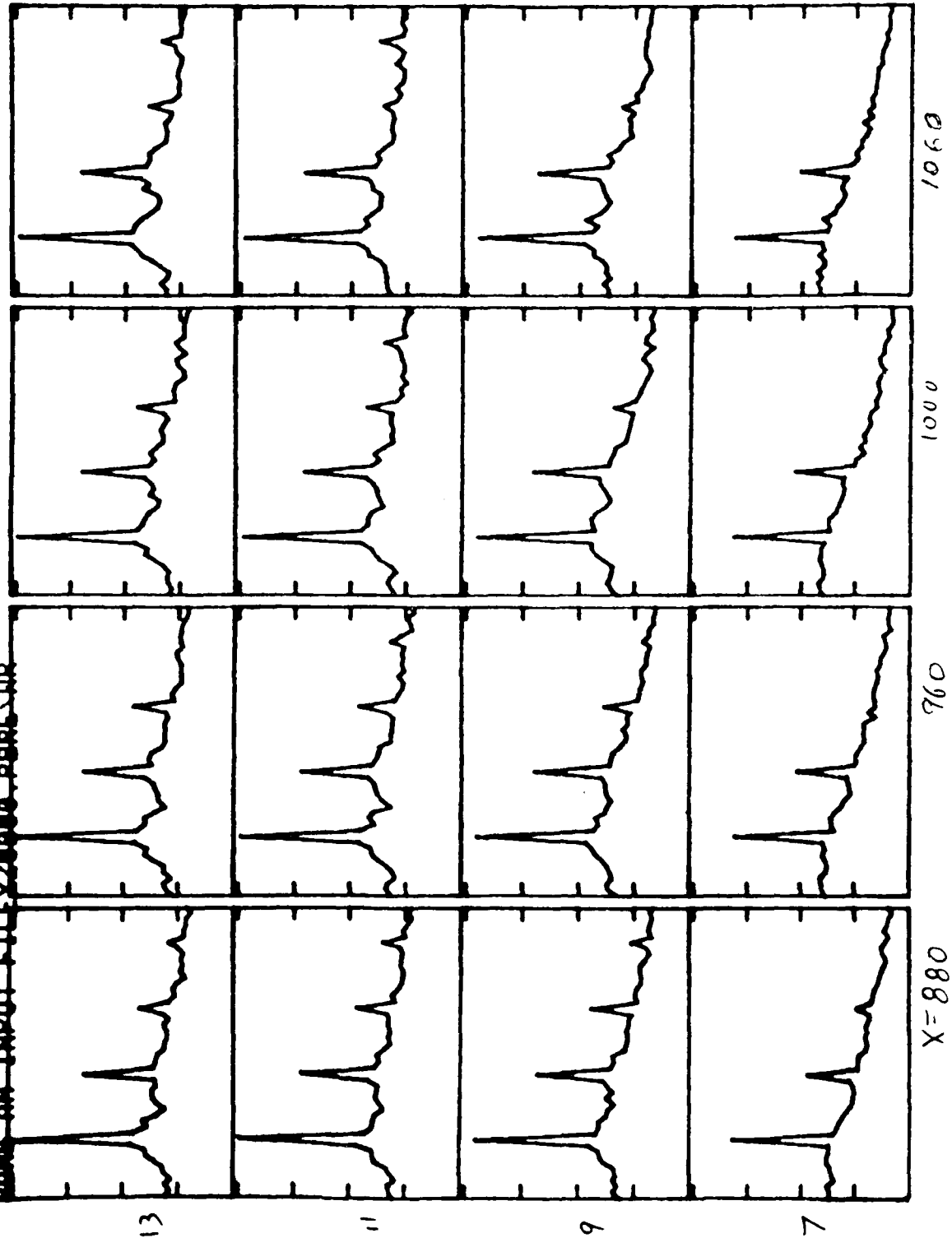


Fig. 23

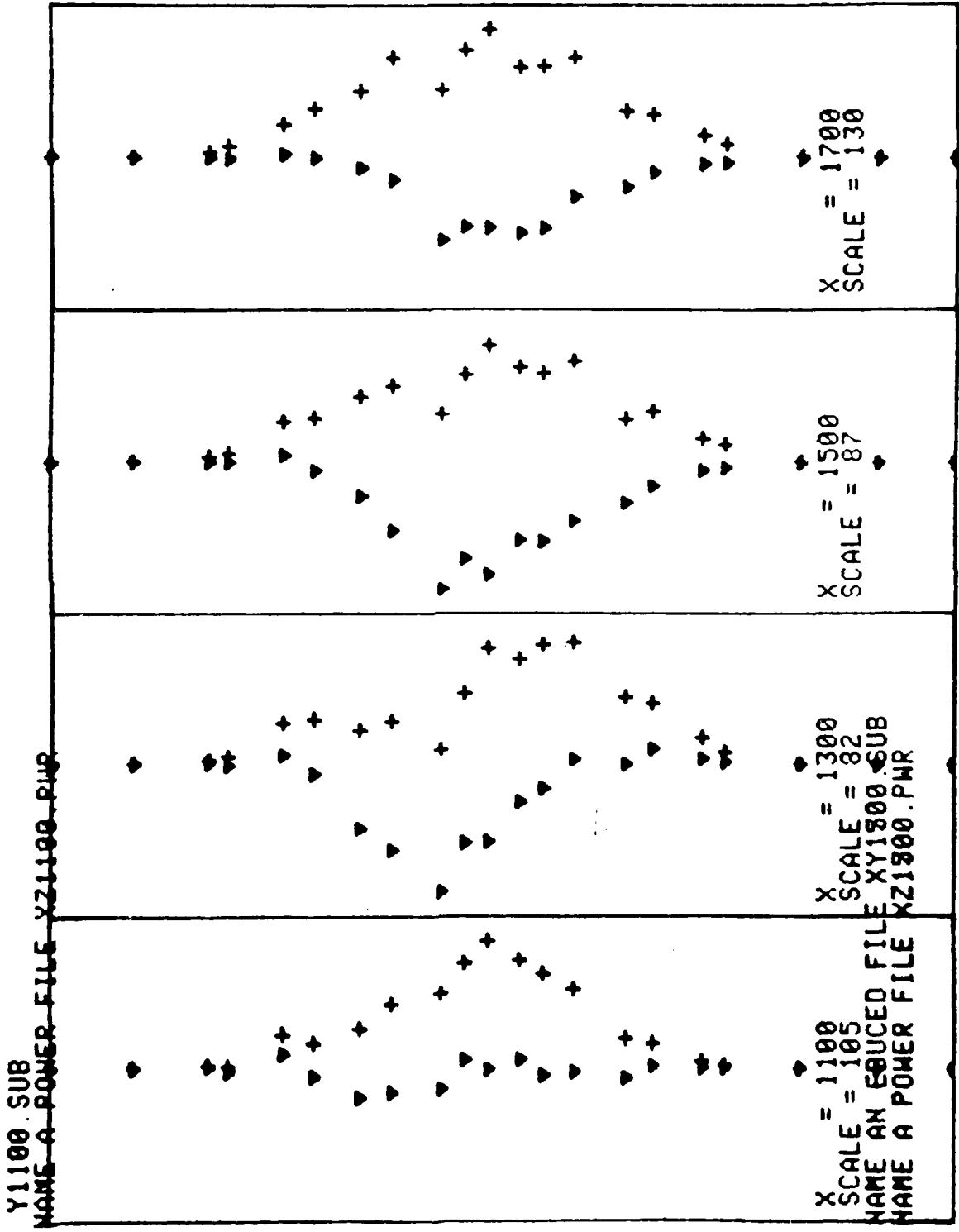


Fig. 24

NAME AN INPUT FILE XZ1100.BBB.PUR S(3) = -0.28863E-1 S(4) = 0.19242E-1

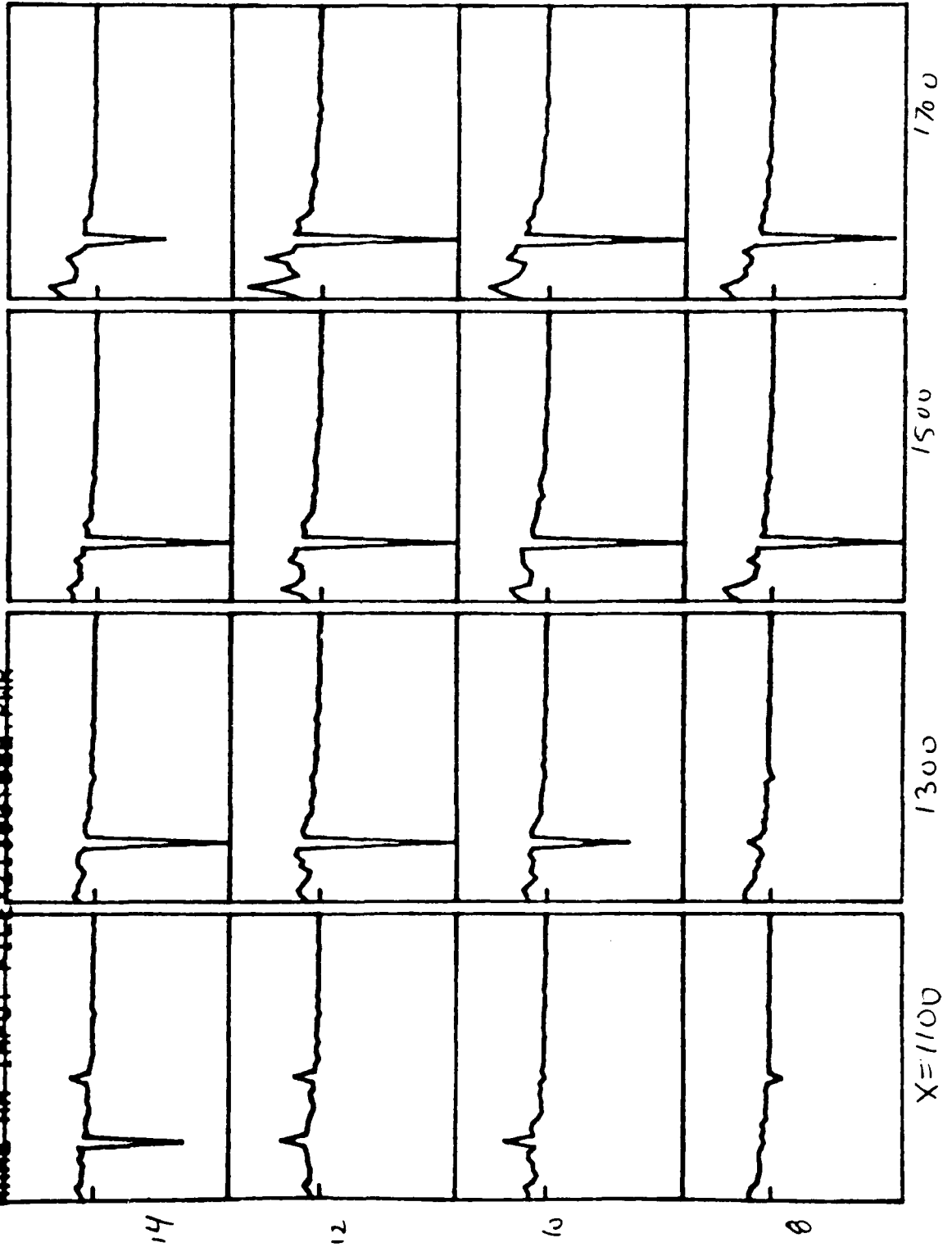


Fig. 25